UNIVERSITY OF LEEDS

METASOMATIC VEIN FORMATION BY STATIONARY FLUIDS IN CARBONATE XENOLITHS AT THE EASTERN MARGIN OF THE BERGELL INTRUSION, VAL SISSONE, ITALY

Bégué F.*, Institute of Earth Sciences, University of Lausanne, 1015 Lausanne, Switzerland.

Baumgartner L. P., Institute of Earth Sciences, University of Lausanne, 1015 Lausanne, Switzerland.

Müller T., School of Earth and Environment, University of Leeds, Leeds, LS2 9JT, United Kingdom.

Putlitz B., Institute of Earth Sciences, University of Lausanne, 1015 Lausanne, Switzerland.

Vennemann T., Institute of Earth Surface Dynamics, University of Lausanne, 1015 Lausanne, Switzerland.

*Corresponding author. E-mail: Florence.Begue@unil.ch; Phone: +41 (0)21 692 44 45; Fax: +41 (0)21 692 43 05

Running Title: Hydrothermal vein formation by stationary reactive fluid

ABSTRACT

Fluid flow is an important mechanism associated with heat and mass transport within the Earth's crust. The study of veins, which represent channelling of fluids, can thus be key in understanding these fluid movements, unravelling fluid composition and origin, paleo stress regimes, and the history of the host-rock.

New stable isotope data on carbonates and silicates have been combined with phase petrology, mass balance, and field observations to evaluate the formation mechanism of metasomatic reaction veins in dolomitic xenoliths in the Bergell tonalites (Val Sissone, Italy). Multiple generations of extensional veins can be followed from the contact zone between the dolomites and the intrusion to a few meters within either the tonalites (with the epidote-quartz veins), or within the dolomites, where they terminate. Each type of vein contains a central zone, which is formed by open fracture crystallization. This central fracture is framed by relatively symmetric replacement zones, where the original dolomite reacted to form either forsterite, diopside, tremolite or talc, all accompanied by calcite in either a succession of reaction zones or in simpler bi-mineral (silicate + calcite) veins.

The $\delta^{18}O$ and $\delta^{13}C$ values across the veins allow temperatures to be estimated from different mineral pairs (silicate + calcite), and which confirm vein formation along a retrograde cooling path of the intrusion. At least four different fluid infiltration events are required, the first one around 555 °C to form the forsterite-calcite veins, followed by the epidote-quartz veins at temperatures around 430 °C, then the tremolite-calcite veins at around 390 °C, and finally the talc-calcite veins at around 140 °C. The shape of the $\delta^{18}O$ and $\delta^{13}C$ profiles, which are flat across the central part and the replacement zones of the veins (buffered by the intrusion), change substantially over short distances. Both of these isotope profiles overlap with the equally sharp mineralogical front between the veins and the unreacted

dolomites. These profiles are interpreted to be the result of an isotopic exchange mechanism driven by dissolution and re-precipitation reactions.

All veins are oriented perpendicular to the contact with the intrusive body, except for the late talc veins. Elevated fluid pressures, above the confining pressures caused by the regional and intrusion emplacement stress field, are suggested to be responsible for the initial fracturing of the carbonates and intrusive rocks. The contact zones between the tonalites and carbonates likely served as fluid conduits, where fluids accumulated and the pressure built up until hydrofracturing occurred. We propose that the veins formed through episodic pulses of highly reactive fluids that remained stationary during reaction, rather than a system where fluids flushed through the veins. Based on the X_{CO2}-constrained mass balance, the formation of the veins would only require a relatively small amount of fluid, which could potentially originate from the intrusive rocks in vicinity of the xenoliths. Veining is not ubiquitous around the Bergell intrusion, suggesting that it only may have been a localized event and thus there is no need to involve a larger convective hydrothermal system for their formation.

KEYWORDS: hydrofracturing; metasomatic veins; reactive flow; skarn; stable isotopes

INTRODUCTION

Fluid movements are an effective heat and mass transport mechanism within the Earth's crust (e.g. Person and Baumgartner, 1995). These movements have received a lot of interest in the study of ore-forming systems, as they are suggested to play an important role in concentrating the ore. To better understand their role in crustal processes, it is essential to study the rocks that have interacted with fluids, as these rocks can preserve a record of the fluid composition and origin, as well as where and why those fluid movements occurred. Channelized fluid flow along veins plays a key role in facilitating these fluid movements. When the fluid is out of chemical and/or thermal equilibrium with the host-rock, transformation and reaction of the latter can occur, where original phase assemblages may progressively change their chemical composition or may even be fully replaced by new minerals (e.g. Holness, 1997; Bowman *et al.*, 2009; Müller *et al.*, 2009; Penniston-Dorland *et al.*, 2010; Ferry *et al.*, 2011; Putnis and Austrheim, 2013; Jonas *et al.*, 2014, 2017). These reactive transport processes therefore govern the chemical, isotopic and thermal evolution of the crust, and at a broader scale even affect large-scale volatile cycles (e.g. Kerrick & Caldeira, 1998; Jamtveit & Austrheim, 2010). A quantitative understanding of the conditions under which these reaction zones form and how much reactive fluid is required is pivotal. Yet, the extent of fluid flow at crustal levels is not always well constrained. Some metamorphic terranes provide evidence for efficient fluid-conduits on the kilometre-scale involving long-distance transport of chemical elements (e.g. Ferry, 1992; Oliver *et al.*, 1993; Cartwright *et al.*, 1995; Penniston-Dorland and Ferry, 2008). However, many vein networks also form through infiltration of locally-derived and modest amounts of fluids (e.g. Burkhard and Kerrich, 1988; Yardley and Bottrell, 1992; Cartwright *et al.*, 1994; Yardley, 2009) but still produce significant reaction zones.

4

The combination of different chemical and stable isotope data is widely used to trace metamorphic fluid–rock interactions and thus provide valuable information about possible sources of the fluids, reaction temperatures, and mass transfer mechanisms (e.g. Skelton et al., 2000; Penniston-Dorland et al., 2010; Baumgartner & Valley, 2001; Nabelek, 2002; Müller et al., 2004, 2009; Bowman et al., 2009; Ferry et al., 2010). This method is particularly effective for metasomatized carbonates during contact metamorphism, as there is a large isotopic and chemical contrast between the igneous rocks and the sediments, thus facilitating the tracing of the fluids (e.g. Bowman *et al.*, 1994; Gerdes *et al.*, 1999; Ferry *et al.*, 2001; Müller *et al.*, 2004, 2009; Durand *et al.*, 2006; Nabelek, 2007). Such data-sets allow determination of the driving forces of the metamorphic/metasomatic reactions. A thorough in situ analysis of the spatial distribution, connectivity and/or intersection of the vein network is crucial to understand the geometry of the fluid flow. While this information is often unavailable, the vein network evaluated in this study is remarkably well exposed and thus perfectly suited for this kind of analysis.

This contribution focuses on metasomatic reaction veins formed in dolomitic xenoliths at the eastern border of the Bergell intrusion (Italy; Fig.1). These veins, including a central open fracture-fill and associated reaction zones, are related to post-intrusion hydrothermal activity during cooling (Bucher-Nurminen, 1981). Note that in this study, we use the term "vein" to describe the central fracture and the associated reaction zones. There are multiple generations of extensional veins within the xenoliths and the surrounding tonalites that form through infiltration of fluids of magmatic origin that interact with the carbonates. These veins can be traced from the contact zone to a few meters within either the tonalites (occurring as epidote-quartz veins), or the dolomites (Fig. 2a, b and d), exposing forsterite-calcite, tremolite-calcite, and talc-calcite veins, or even more complex composite veins (e.g. Fig. 3; Bucher-Nurminen, 1981). Building on previous work (e.g. Bucher-Nurminen, 1981; Taylor &

Bucher-Nurminen, 1986; Bucher, 1998), new stable isotope analyses on silicates and carbonates were acquired, and the results were combined with field observations, structural analyses and theoretical mass balance constraints to advance our understanding on the formation mechanism of these veins, their fluid source and volume, and extent of isotopic exchange. In contrast to the formation model suggested by previous authors (Bucher-Nurminen, 1981; Taylor & Bucher-Nurminen, 1986; Bucher, 1998), in which large amount of fluids flushed through the system, we present convincing evidence for an interpretation that supports vein formation by more localized fluid infiltration events, through infiltration of relatively small amounts of fluids that remain stationary during metasomatic exchange.

GEOLOGICAL SETTING

The Bergell intrusion (Central Alps, Northern Italy) represents one of the rare examples of Tertiary magmatism in the European Alps (e.g. Wenk, 1973; Trommsdorff and Nievergelt, 1983; Schmid *et al.*, 1996a; Rosenberg, 2004; Fig. 1). It intruded the Penninic and Austroalpine basements and nappes, which are characterized by a poly-phased alpine regional metamorphism predating a contact metamorphic event (e.g. Trommsdorff & Connolly, 1996). The intrusion is wedged between two major faults: the Engadine line to the North and the Insubric line to the South (Fig. 1; e.g. Rosenberg *et al.*, 1995; Berger *et al.*, 1996; Rosenberg, 2004). These two alpine faults governed the emplacement of the pluton and its subsequent tilt (Rosenberg et al., 1995; Berger et al., 1996; Rosenberg, 2004). Based on numerous field and geochemical observations, it has been suggested that the exposure of the Bergell pluton represents a tilted ≥10 km mid-crustal section (e.g. Rosenberg et al., 1995; Berger et al., 1996; Davidson et al., 1996), with deeper portions of the magmatic system exposed to the West.

The Bergell is a composite intrusion representing a typical calc-alkaline suite (e.g. Trommsdorff & Nievergelt, 1983), with two main units that dominate the exposed pluton

area; (1) a granodiorite, with K-feldspar megacrysts, representing the central part of the intrusion; and (2) a ~5 km thick tonalite rim, surrounding the granodiorites and forming a "tail" towards the West (Fig. 1). At the eastern margin, there is a clear contact between the tonalites and the granodiorites, but towards the West and South, a common magmatic history of the tonalites and the granodiorites is indicated by the presence of a texturally hybrid granite forming a transition zone (i.e. the "Übergangszone" of Moticska, 1970; Trommsdorff and Nievergelt, 1983; Hermann *et al.*, 2006; Gianola *et al.*, 2014; Samperton *et al.*, 2015). A recent study by Samperton et al. (2015) determined zircon crystallization ages with a range from ~31.9 to 30.3 Ma, with the tonalites being older than the granodiorites, in accordance with previous ages (von Blackenburg, 1992). A protracted zircon crystallization over 1.6 Ma and the production of increasingly evolved magmas through combined fractional crystallization and crustal assimilation was suggested on the basis of the geochronology data with textural imaging, and trace element geochemistry of the zircons (Samperton et al., 2015). The Bergell intrusion also shows evidence of an incremental assembly, with the tonalites likely to have crystallized from two distinct magma reservoirs (von Blanckenburg et al., 1992; Samperton et al., 2015). Younger aplitic and pegmatitic dykes crosscut the different intrusive units.

In this study, we focus on the eastern margin, which represents the top portions of the Bergell pluton. Here, the intrusion of magmas caused a ~1.5 to 2 km thick contact aureole (Trommsdorff & Evans, 1972) that overprints a greenschist facies regional metamorphism (~350 °C; Trommsdorff & Connolly, 1996). A detailed study on the structures of this eastern margin was presented by Berger & Gieré (1995), who showed predominant syn- and some post-intrusive deformation, using indicators like folded dykes, boudinaged sills, lineation or aspect ratio of mafic enclaves. A flattening –type of strain has been commonly described when referring to the mafic enclaves in this part of the Bergell intrusion (Berger & Gieré,

1995). The contact metamorphic mineral assemblage observed in metapelites from the pre-Mesozoic Suretta basement (garnet + sillimanite + cordierite + biotite + muscovite + alkali feldspar + plagioclase + quartz) suggests pressure and temperature conditions of ~0.35 GPa and ~700 °C (Wenk et al., 1974). Contact metamorphism of ultramafic rocks yielded an assemblage of anthophyllite + olivine, and enstatite + olivine indicative of temperatures in excess of 650 °C and 0.3 GPa at the contact (Trommsdorff & Evans, 1972). We note that the pressures obtained using equilibrium phase relations are lower than estimates derived from Al-in-hornblende geobarometry (0.45-0.65 GPa) for the eastern margin of the Bergell (Davidson et al., 1996). However, amphibole crystallization likely records deeper parts of the magmatic plumbing system with subsequent ascent to shallower depths by the magma. Fluid flow during peak contact metamorphism has been constrained in ophicarbonates by Ferry (1995); a large amount of fluids has been suggested sourced from devolatilization reactions in the host rock.

Within the tonalitic rim, at the eastern margin, many elongated, lenticular-shaped carbonate xenoliths (10 – 100 m long, 1-20 m wide) of calcsilicate and dolomitic nature are present (Fig. 2a and b; e.g. Bucher-Nurminen, 1981; Gieré, 1985). They are suggested to belong to the Mesozoic sedimentary cover of the Suretta Nappe (Fig. 1), which is located to the north-east and east of the Bergell intrusive body (Gieré, 1985). Contact metamorphism produced a calcite-dolomite-forsterite-clinohumite-spinel-phlogopite assemblage within the originally impure siliceous dolomites (Bucher-Nurminen, 1981). Skarns forming at the contact between the marbles and the intrusive rocks, and metasomatic reaction veins, cross-cutting both the sedimentary and intrusive rocks (e.g. Bucher-Nurminen, 1981) overprint the contact metamorphism. These features are the main topic of this study.

FIELD OBSERVATIONS

The Bergell carbonate xenoliths and metasomatic reaction veins were intensely studied during the early 1980's (Bucher-Nurminen, 1981, 1987, 1989; Taylor and Bucher-Nurminen, 1986; Bucher, 1998). Much of the groundwork on the textures and field observations was established by Bucher-Nurminen (1981). The author interpreted the composite veins as a succession of reaction zones; each reaction zone having two major phases: calcite and, in a succeeding order from the carbonate host rocks towards the vein centre, either forsterite, diopside, tremolite, or talc (Fig. 3). These reaction zones are also present as simpler bi-mineral veins, with calcite and one of the above-mentioned silicates; these veins are the main focus of this study. The only exception is diopside, as no simple diopside + calcite veins were found in the field. Diopside is only present in the complex composite veins, and it is suggested to be produced from tremolite reacting with calcite under Fe- and Al- enriched conditions (e.g. Bucher-Nurminen, 1981).

Structural Observations

The main orientation of the structures is the SSE-NNW direction (Fig. 4), reflected by the original sedimentary layering of the carbonates (s0) and the contact zones between the xenoliths and the tonalites, which are nearly vertical. A hornblende lineation, and the elongation and alignment of the mafic enclaves, observed within the tonalites close to the contact, also follows this orientation. The s0 of the xenoliths and s0 of the country rock also have the same orientation (data from Berger and Gieré, 1995; Fig. 4b), indicating a common deformation event, and suggesting that the xenoliths were re-oriented together with the host-rock. A second general orientation (NNE-SSW direction), which is nearly perpendicular to the first one, is defined by the majority of the metasomatic veins (Fig. 4a). These veins also formed perpendicular to the contacts between the tonalites and the dolomites, and some can

actually be directly linked to the contact zones (Fig. 2a, b and d). Taken together, these observations suggest that a uniform stress regime was present at the time of metasomatic vein formation. In contrast, the talc veins show a larger spread in orientation (Fig. 4a), representing a more variable stress regime. Nevertheless, some talc veins are shown to share the same orientations as the other veins, suggesting that some of those veins have replaced existing tremolite veins.

The presence of the epidote-quartz veins in the tonalites is evidence for sub-solidus brittle fracturing of the intrusive rocks, during the formation of the veins. Minor shearing (predominantly sinistral) can also be observed along the metasomatic reaction veins, evident from small displacements of sedimentary layers across the veins (e.g. Fig. 5a). Furthermore, thin (<0.5 mm), sheared zones with microcrystals (0.01 mm) of calcite are occasionally present at the vein boundaries between the original dolomite and the tremolite zone (Fig. 5b and d).

Geology and Mineralogy of Contact Skarns and Metasomatic Veins

The simpler bi-mineral veins are divided into four different groups for the following in-depth petrographic and isotopic study: (1) an epidote-quartz vein including its endoskarn forming within the tonalites (Fig. 2e); (2) a forsterite-calcite vein (Fig. 5a and e); (3) a Fe-poor tremolite-calcite vein (Fig. 5b, d and f-g), as well as a Fe-rich tremolite-calcite vein (Fig. 6); and (4) a talc-calcite vein (Fig. 5c). Prior to a detailed description of the veins, we will briefly characterize the dolomitic marbles of the carbonate xenoliths and the skarns forming at the contact with the tonalites (Fig. 2c and d).

Carbonate Xenoliths

Dolomitic marbles constitute most of the carbonate xenoliths (Gieré, 1985) and host the metasomatic reaction veins (Fig. 2). These are commonly massive, and consist of 90-95 vol.% idiomorphic dolomite, with a grain size from 0.25 to 1.5 mm. The remaining mineral assemblage is made up of calcite, spherical olivine, diopside, and titanoclinohumite. Original sedimentary layering is well preserved, with mm to cm-wide silicate-rich layers, mainly composed of fine-grained (0.1 mm) phlogopite, some titanoclinohumite, olivine and spinel, in a calcite matrix (Fig. 5a-b). Those layers may be discontinuous and irregularly spaced. Some of the smaller dolomitic xenoliths (<1 m) were completely transformed into skarn.

Contact Skarns

Skarns forming at the contact between the dolomitic marbles with the tonalites received much less attention in the past compared to the metasomatic reaction veins forming within the xenoliths, because a prolonged history of crystallization caused the high-temperature metamorphic assemblage to be retrograded. Nevertheless, a contemporaneous formation has been suggested for these skarns and the reaction veins, based on a similar succession of reaction zones (Bucher-Nurminen, 1981). These reaction zones form parallel to the contact (Fig. 2c and d). The thickness of the skarns is variable and ranges from a few centimetres up to a meter in thickness, and the presence, size and mineral mode of each reaction zone is highly variable among the different contact zones between the carbonates and the tonalites. A typical mineral sequence, from the carbonate towards the tonalite, is as follows; an outer reaction zone consisting of olivine and calcite, with dolomite remaining stable as isolated grains (Fig. 2c). The following zone consists predominantly of tremolite and calcite, with amphiboles being pseudomorphs after diopside, which itself remains preserved in some contact skarns. Quartz, alkali-feldspar and plagioclase crystals are the predominant

mineral phases of the following zone, which is likely already part of the endoskarn (Fig. 2c).

Finally, there is a gradual transition to a last zone (endoskarn), which is texturally similar to

the tonalites, exposing diopside pseudomorphs after hornblende and an increased presence of

hornblende relicts towards the original tonalites. The interpretation of hornblende being

replaced by diopside is supported by the presence of titanite, as the immobile element Ti is

not as easily incorporated into the pyroxene structure compared to the amphiboles. Generally,

the contact skarns are altered with a late generation of amphibole, serpentine, talc and chlorite

representing the abundant alteration products.

Epidote-Quartz Veins

The epidote-quartz veins (Fig. 2e and f) form within the intrusive rocks approximately

perpendicular to the igneous contact. They are parallel to the metasomatic reaction veins in

the carbonates (Fig. 2d). Texturally they can be divided into a central zone, characterized by

open fracture crystallization, and a replacement zone where the original igneous textures is

maintained (endoskarn; Fig. 2e). Macroscopically, the transition from the open fracture to the

replacement zone is sharp. Microscopically, it is, however, typically more gradual and

associated with a decrease in grain size (from ~2 mm to ~0.5-1 mm) over a few millimetres.

The mineral assemblage of the central zone is dominated by idiomorphic cm-sized epidote

and quartz grains. Epidote is often twinned and commonly crosscut by small quartz and

calcite veinlets. Idiomorphic calcite grains are observed towards the contact with the

dolomites, but otherwise calcite is mostly interstitial.

The endoskarn shows similarities with the endoskarn from the contact zone and can

broadly be subdivided into two distinct zones. In the first zone next to the central zone, quartz

and calcite are either present as large interstitial domains, or, along with epidote, form small

veinlets crosscutting plagioclase, alkali feldspar and an earlier generation of rounded quartz

(Fig. 2f). Fibrous actinolite exhibits intergrowth textures with calcite (Fig. 2f), commonly accompanied by the presence of titanite. In addition, biotite is replaced by chlorite. The fibrous actinolite, as well as chlorite, represent a second generation of mineral replacement of the original endoskarn assemblage. The second, outer zone of the endoskarn, close to the non-metasomatized tonalitic rock, is characterized by a gradual disappearance of interstitial quartz, epidote and calcite, and a gradual increase in biotite grains towards the tonalites. Actinolite is not fibrous anymore, and forms pseudomorphic replacement after hornblende, with some hornblende relicts present towards the unreplaced tonalites. Quartz and both feldspars form the more usual igneous texture of the tonalites.

Metasomatic Reaction Veins in the Dolomitic Xenoliths

Reaction veins are abundant within the dolomitic marbles. Field observations indicate that their occurrence, as well as that of the epidote-quartz veins, are directly linked spatially to the contact skarns (Fig. 2d). Multiple reaction types can be discerned forming recurring sequences with some variability in size (cm to multiple dm), chemical composition (e.g. Fe-content) or degree of alteration, as described by Bucher-Nurminen (1981). Regardless of the observed variations, they collectively share the presence of two distinct zones: (1) a central zone, which is defined by textures resulting from open-fracture crystallization, indicative of fluid infiltration (e.g. Bucher-Nurminen, 1981). The thickness of this zone can range from <1 mm to a few cm thick, depending on the vein. (2) a replacement zone, which frames the central zone on both sides, and in which the original carbonates have been replaced by new minerals forming variable assemblages (Figs. 5-6). The following sections provide petrographic descriptions of the bi-mineral veins, which have been chosen for detailed isotopic analysis.

The forsterite-calcite veins are characterized by a sharp mineralogical front exhibiting an undulated or lobed morphology (Fig. 5a; Bucher, 1998). In the replacement zone the textures are homogeneous, with forsterites of an average size of 0.25 mm in diameter (albeit some grains exceeding 2 mm), commonly twinned, and often forming clusters that are surrounded by sub-millimetric calcite crystals (Fig. 5e). Scarce isolated grains of dolomite are still present throughout the replacement zone. The original sedimentary layering of the carbonates defined by phlogopite-rich layers, is preserved throughout the replacement zone (Fig. 5a). Preservation of this layering is evidence that this zone formed through replacement, whereas the central zone lacks this layering and is hence a fracture fill (Fig. 5a). The phlogopite in these layers can be replaced by chlorite and tremolite. These layers appear to represent a barrier to the forsterite and calcite reaction, as the thickness of the replacement zone in the dolomitic regions decreases well before approaching one of those layers, as can be observed in Figure 5a. The extent of the central zone is typically very thin (0.25-0.75 mm, Fig. 5a), where forsterite is commonly replaced by late talc and chlorite. Retrograde serpentinisation is also observed in fractures and along grain boundaries of some forsterite grains. In addition, inclusions of serpentine needles accumulating along cleavage planes and grain boundaries of the calcite can be found.

The mineralogical front of the tremolite veins is straight compared to those observed in forsterite veins (Fig. 5b and d; see also Bucher, 1998). They also show a diversity in composition, from Fe-poor (white) to Fe-enriched (green) minerals (Fig. 6), and textures, with tremolite habits ranging from sub-mm fibres to 10 cm long prismatic crystals (Fig. 5f-g). The Fe-poor tremolite vein (vein 06-L2 in Fig. 5b-d; samples 06-L2-16 and 06-L2-12) exhibits some clear textural changes between the replacement and the central zone. The replacement zone is characterized by a dense aggregation of small fibrous and radiating clusters of tremolite (avg. size 0.25 mm), with small interstitial calcite grains (0.1 mm; Fig. 5g). The

crystal size increases towards the central zone, characterised by the presence of large (6 -7 mm) elongated fibres of tremolite and mm-sized calcite grains (Fig. 5f). Similar to the forsterite vein, the transition from the replacement to the central zone is marked by the discontinuation of the original sedimentary layering (Fig. 5d). The thickness of the replacement and the central zone decreases gradually towards the tips of the vein, with the central zone thinning out to a <1 mm fissure with late talc replacement (Fig. 5b). Retrograde talc and chlorite are also common across the vein.

In the Fe-enriched tremolite veins (Fig. 6a), the replacement zone consists of small fibrous and radiating clusters of tremolite with crystal size increasing towards the central zone similar to textures observed in the Fe-poor tremolite veins. The Fe-replacement front can be easily followed, due to the green coloration of the amphiboles. On the outcrop scale, this coloration, commonly lags behind the mineralogical front. The secondary chemical replacement involving Fe is visible in the elemental maps, showing clear zoning of tremolite crystals, with a rather sharp increase in Fe from core to rim, and an enrichment of Fe in the central zone relative to the replacement zone (Fig. 6b). This enrichment is also correlated with an Al_2O_3 increase (Bucher-Nurminen, 1981).

The last vein generation crosscuts all other veins. They are the talc veins, which are abundant, and usually only a few cm thick. Rhythmic textures are common, as can be observed in Figure 5c, with a succession of thin (mm) talc-rich bands, interspaced with more calcite-rich bands. Talc textures in several veins suggest a pseudomorphic replacement after the tremolite. The vein chosen for this study (sample 07-L30-1) is one of these examples. The textures are similar to the ones of the tremolite vein, with a gradient from very fine-grained talc clusters (~0.05 mm) and calcite crystals in the replacement zone, to a coarsening of the minerals towards the central zone (0.25-1.3 mm).

All field observations are integrated into our final vein formation model. Nevertheless, to further understand the vein formation mechanisms, we chose four bi-mineral veins (forsterite-calcite, Fe-poor tremolite-calcite, talc-calcite, and epidote-quartz veins) for stable isotope analyses. The essential observations regarding these veins are that all have a central zone representing open-fracture crystallisation, where either forsterite, tremolite or talc precipitated along with calcite. This zone is surrounded by a replacement zone where the dolomite from the carbonate xenolith reacted to form the same mineralogy as in the central zone. The epidote-quartz veins forming in the tonalites have the same structure, with open-fracture crystallization in the centre and a replacement zone of typical endoskarn.

ANALYTICAL METHOD

Simple bi-mineral veins from the carbonate xenoliths, an epidote + quartz vein from the tonalites, and a complex vein were selected for this study, with a total of 27 samples (hand-samples and drill cores of 4.5 cm diameter and 10-20 cm length). They represent complete transects across the different vein types (total of 19 transects in 4 forsterite-, 8 tremolite-, 3 epidote-quartz-, 1 talc-, and 3 complex-veins), and they include three different contact zones between dolomites and tonalites. These samples were cut perpendicular to the vein or the contact zone. Calcite was stained in thin sections and hand specimens to distinguish it from dolomite at the hand-sample and microscopic scale, following the procedure described in Hutchison (1974). All data presented in this study have been acquired at analytical facilities available at the University of Lausanne (Switzerland).

$\delta^{18}O$ and $\delta^{13}C$ - Carbonates

Oxygen and carbon isotope compositions have been analysed along profiles perpendicular to the vein centre for one forsterite vein (07-L18-4B), two Fe-poor tremolite

16

veins (06-L2-16 and 06-L2-12), one Fe-enriched tremolite vein (07-L18-2), and one talc vein

(07-L30-1). Using a micro-drill, small amounts of powder were extracted every few

millimetres along a profile perpendicular to the reaction vein. Sample size varied between 100

and 500 μg, depending on the calcite to dolomite ratio estimated from the petrography. $\delta^{18}O$

and $\delta^{13}C$ values were measured with a Thermo Finnigan Gas Bench, coupled to a DeltaPlus

XL mass spectrometer. Complete reaction of the carbonates (dolomite and calcite) was

ensured using 100 % phosphoric acid, with acid and samples heated to 90°C. Helium was

used as the carrier gas for the produced CO_2, following the method described in Spötl &

Vennemann (2003). Acquired oxygen and carbon isotope compositions were measured with

respect to the Carrara Marble international standards, and are reported relative to VSMOW

(Vienna Standard Mean Ocean Water) and VPDB (Vienna Peedee Belemnite), respectively

after Craig (1957). The accuracy over the entire analytical session was typically 0.05-0.06 ‰

(1sd) for $\delta^{13}C$ and 0.06-0.08 ‰ (1sd) for $\delta^{18}O$ as estimated from replicate analyses of samples

and standards.

$\delta^{18}O$ - Silicates

Silicates have been separated from traverses across one forsterite vein (07-L18-4B),

one Fe-poor tremolite vein (06-L2-16), and one talc vein (07-L30-1) following the method

described in Müller et al. (2004). We cut thick sections (300 μm), oriented perpendicular to

the vein, into 1x1 mm squares paralleling the vein, using a diamond wire saw (diameter of the

wire 170 μm). As about 1 mg of material was required for the laser fluorination analysis, we

selected multiple squares, equidistance from the vein front, to yield sufficient silicate material

(i.e. five squares for the olivine vein, and three squares each for the tremolite and talc veins).

Hydrochloric acid (15%) was used to dissolve the carbonates (about 10 min.) except for the

forsterite vein, for which we used acetic acid (20%) for complete dissolution of the carbonates

(~150 min) was observed. Forsterite, tremolite and talc from each sample was then

handpicked from the silicate residue. Powders of epidote and quartz from the vein 07-L2-23

were extracted using a micro-drill, given their large crystal size. Oxygen isotopes of the

silicates were measured with a CO_2 laser-based extraction line and F_2 as a reacting gas (e.g.

Rumble and Hoering, 1994; Lacroix and Vennemann, 2015), coupled to a Finnigan MAT 253

mass spectrometer. The data was collected in blocks of 12 analyses each, where either the

NBS-28 quartz ($\delta^{18}O$ = 9.64 ‰; Coplen *et al.*, 1983) and the in-house LS-1 quartz ($\delta^{18}O$ =

18.1 ‰) standards were analysed twice at the beginning and once at the end of each block.

The data were reported relative to VSMOW; the standard deviation was typically better than

0.2 ‰ (1sd), based on replicate analyses of samples and standards.

δD - Hydrous Silicates

Tremolite from the Fe-poor vein 06-L2-16, and talc from the vein 07-L30-1 separated

for $\delta^{18}O$ analysis were used to measure δD. The hydrous silicates were tightly folded into

silver capsules. The sample size required for an analysis depends on the amount of water in

the given mineral and was typically 2 to 2.5 mg for tremolite and 1.5 to 2 mg for talc,

respectively. Hydrogen isotope compositions were measured using a Finnigan MAT high-

Temperature Conversion – Elemental Analyzer (TC-EA) coupled to a DeltaPlus XL mass

spectrometer, following the analytical method described in Vennemann et al. (2002). Two in-

house standards; G1 biotite (δD = -66 ‰) and K-17 kaolinite (δD = -125 ‰) have been used

to normalise the measured isotopic composition (Vennemann and O'Neil, 1993). They were

measured several times (5-10) at the beginning and at the end of the analysis block of 10-15

unknowns. Raw δD values were reported relative to VSMOW international standard. The

accuracy of analysis was better than 2 ‰ (1sd), based on replicate analyses of samples

and standards.

STABLE ISOTOPE COMPOSITIONS

The stable isotope analyses are listed in the Tables 1-3. All isotopic compositions of

the carbonates are presented in Figure 7, and the $\delta^{18}O$ values have a range from +12 to +25

‰, and $\delta^{13}C$ values from -7 to +1.5 ‰. Most values cluster in two groups, a low $\delta^{18}O$ - $\delta^{13}C$

group, corresponding to the calcite in the vein, and a high $\delta^{18}O$ - $\delta^{13}C$ group representing the

dolomitic protolith, with only a few values in between. The profiles across the respective

veins show very similar patterns (Fig. 8 and 9), which can be described by: (1) a flat profile of

low $\delta^{18}O$ and low $\delta^{13}C$ values across the central part and the replacement zones of the veins;

(2) a sharp increase of the stable isotope composition corresponding to the location of the

mineralogical replacement front; and (3) a flat plateau with high $\delta^{18}O$ and $\delta^{13}C$ values within

the dolomitic host rock. Taylor & Bucher-Nurminen (1986) analysed similar isotopic fronts

across a tremolite and a more complex composite vein. The different values present at the

"isotopic fronts" (Fig. 8 and 9), plot along the mixing line in Figure 7 (except for the forsterite

veins, which will be discussed in the "Isotope Exchange Mechanism" section). This line

represents an artefact of the sample preparation method using the microdrill resulting in

mechanical mixing between calcite and dolomite; since calcite and dolomite have the same

amount of carbon to oxygen ratio, the physical mixing of the vein calcite with the unreacted

dolomites will always result in values plotting along a straight line in a $\delta^{18}O$ - $\delta^{13}C$ plot (Fig.

7). As we used a micro-drill to sample the carbonates for isotopic analysis, we do not have the

spatial resolution to separate single calcite or dolomite grains at the reaction front.

Measured oxygen isotope ratios of the silicate minerals (Table 2) are fairly

homogeneous, with flat $\delta^{18}O$ profiles across the analysed veins (Fig. 8 and 9), similar to the

measured isotope profiles within the carbonates. Forsterite $\delta^{18}O$ values range between 9.0 to 11.1 ‰. Tremolite, epidote and quartz have a slightly narrower range, with 8.2 to 9.1 ‰ for tremolite, 7.3 to 7.7 ‰ for epidote, and 10.7 to 11.9 ‰ for quartz. Talc has a $\delta^{18}O$ range between 8.8 and 12.4 ‰. This variability, with, for instance, a ~2 ‰ variation in $\delta^{18}O$ across the forsterite vein (i.e. Fig. 8), may be related to contamination through mixed analyses with other silicate phases (e.g. serpentine, phlogopite, rare tremolite, chlorite and talc; some of the forsterite also has a humite core). The isotopic composition would be strongly affected by even minor contamination, as some of those minerals are related to late crystallization at lower temperatures and have very different isotopic compositions (e.g. serpentinisation of the forsterites).

Finally, hydrogen isotope analyses were measured on tremolite and talc grains from the same veins used for oxygen isotope analysis (Table 3). The resulting data for the tremolites plot in a tight cluster around -69 ‰. The talc data show a small range with δD ranging from -58 to -69 ‰.

Temperature Estimates

The equilibrium isotope fractionation between co-existing minerals varies as a function of temperature and chemical composition of the minerals (e.g. Clayton & Epstein, 1961; Chacko et al., 2001). The much lower and relatively homogeneous isotopic compositions of the vein minerals suggest an approach to isotope exchange equilibrium; hence, the oxygen isotope fractionation between two coexisting minerals from the reaction veins can be used as a thermometer. We chose experimental and semi-empirical calibrations for apparent equilibrium temperature estimates for the Bergell veins (Matthews & Schliestedt, 1984; Chiba et al., 1989; Zheng, 1993b; Zheng et al., 1994a, 2004), and Δ_{a-b} as an approximation for $10^3 ln\alpha_{a-b}$ (a and b representing two minerals at equilibrium; Rumble,

1982). To calculate Δ_{a-b}, we paired a carbonate data point to a silicate one analysed in close proximity at equidistance to the vein boundary (c.f. Table 1 and 2). Figure 10 shows the range of the measured Δ_{a-b} values (in ‰) across the replacement and central zone of the respective veins, with the black line being the median, the lower and upper shaded boxes the 25th and 75th percentile, respectively, of these Δ_{a-b} values. Dashed horizontal lines represent the minimum and maximum Δ_{a-b} value. Small variability in Δ_{a-b} values is mostly due to sampling artefacts, related to minor contamination of the silicate material, as explained above, and to the fact that the sample volume between the silicates and the carbonates required for analysis is very different. Where applicable, various calibrations have been used (Fig. 10 a, b and d), which in all cases yield similar results. We note that none of the experimental calibrations have been established for such low temperatures as obtained for the tremolite vein.

Measured oxygen isotope fractionations indicate average formation temperatures of 555 °C (507-645 °C) for the forsterite vein, 430 °C (410-485 °C) for the epidote-quartz veins and 390 °C (295-485 °C) for the tremolite veins, respectively (rounded to the nearest 5 °C; Fig. 10). The apparent equilibrium temperature of talc veins is the lowest at approximately 140 °C, but varies from 50 to 230 °C (Fig. 10 c). The isotope thermometry data are in fair agreement, albeit slightly higher, than the ones based on the calcite-dolomite thermometer, with temperatures for the forsterite (~500 °C) and the tremolite veins (~300 °C; Taylor & Bucher-Nurminen, 1986). The discrepancy in calculated temperatures may be explained by variations in X_{Mg} of calcite at the grain scale, related to re-equilibration and exsolution, which has been suggested to impair the accuracy of the calcite-dolomite thermometer (Müller et al., 2008).

DISCUSSION

Infiltration of fluids is required to explain skarn development in contact zones and the spatially connected metasomatic reaction veins (e.g. Einaudi *et al.*, 1981; Einaudi and Burt, 1982; Meinert, 1992; Baker *et al.*, 2004). In the following discussion, we will first use the stable isotope data to discuss the origin of these fluids and the stable isotope exchange mechanisms. Subsequently, the mineral reactions leading to the formation of the veins will be identified, and along with the field observations, we will propose a formation mechanism for the Bergell reaction veins.

Origin of the Fluids

The combination of different stable isotope systems (H, C, O) can be used to decipher the origin of the fluid, and/or to constrain the dominant mechanism for mass transfer and isotopic exchange (e.g. Taylor, 1977; Baumgartner & Rumble III, 1988; Ferry, 1986; Baumgartner & Valley, 2001). In this study, all analysed veins have a similar profile for stable isotope compositional variations in the carbonates and the silicates (e.g. Fig. 8 and 9). The dolomite protolith is the high $\delta^{18}O$, high $\delta^{13}C$ end-member in Figure 7. Its composition is close to typical marine carbonates from the Jurassic period ($\delta^{18}O_{VSMOW}$ about 26 ‰ and $\delta^{13}C_{VPDB}$ about 2.5 ‰; Veizer & Hoefs, 1976). The much lower isotopic compositions measured across the replacement and central zones of the veins support isotopic exchange with an infiltrating fluid with lower $\delta^{18}O$ and $\delta^{13}C$ values (lower left data cluster in Figure 7). For the Bergell metasomatic reaction veins, these fluids would predominantly be of magmatic origin, as has previously been suggested by Taylor & Bucher-Nurminen (1986). Exchange with these fluids shifted the entire mineral-fluid system to lower values. For reference, magmatic fluids have $\delta^{18}O$ values of +6 to +10 ‰, δD values of -80 to -30 ‰ (e.g. Sheppard, 1986; Taylor, 1974), and $\delta^{13}C$ values of -6 to -8 ‰ (Taylor, 1986). In marbles at the contact with the Adamello intrusion (Northern Italy), equivalent stable isotope compositions of the

dolomite protolith and dolomite infiltrated by magmatic fluids have been measured (Gerdes et al., 1999; Müller et al., 2009).

The much lower $\delta^{18}O$ and $\delta^{13}C$ values of the metasomatic veins relative to the dolomite protolith suggest that these veins are largely buffered by externally derived fluids. Accordingly, we calculated the isotopic composition of water and carbon dioxide (Fig. 11 and 12) of a fluid in equilibrium with the different vein minerals, using calcite-water fractionation (or quartz-water fractionation for the epidote-quartz vein) and the above estimated temperatures (fractionation calibrations from Friedman & O'Neil, 1977; Graham et al., 1984; Savin & Lee, 1988; Scheele &Hoefs, 1992; Zheng, 1993a; Zheng, 1993b; Saccocia et al., 2009). The simpler bi-mineral veins are assumed to form over a limited time interval, likely due to a single isothermal fluid infiltration event, without any visible late-stage overprinting of the system. Additionally, since the calculated silicate-carbonate oxygen isotope exchange temperatures are relatively low, the measured isotopic compositions can be considered to record formation temperatures for the veins (Eiler et al., 1993). These temperatures are much lower than the temperatures at which fluid exsolution from a magma occurs. Hence, we estimated the evolution of the isotopic composition of the fluids in equilibrium with the intrusive rocks with decreasing temperatures, assuming fluid to be in equilibrium with igneous quartz values (Figs. 11 and 12a). As a starting isotopic composition for the magmatic fluid, we use a $\delta^{18}O$ of +9.9 ‰ at 800 °C, which has been calculated from the measured value of 8.8 ‰ for the tonalites of the Val Sissone area (von Blanckenburg et al., 1992), using the fractionation calibrations between tonalite and water from Zhao and Zheng (2003). As there are no hydrogen isotope data

available for the Bergell tonalites, we used a typical δD value of -75 ‰ for hornblende in granites and tonalites (e.g. Taylor and Sheppard, 1986). This results in a δD value of -63 ‰ for a magmatic fluid at 800°C (calibration from Suzuoki and Epstein, 1976).

Calculated oxygen isotopic compositions for water in equilibrium with the forsterite and tremolite vein are around 12.5 ‰ and 9 ‰, respectively, which are higher than the suggested fluid values calculated to be in equilibrium with the tonalites (Fig. 12a). This can be explained by the mixing of a magmatic fluid with contribution of oxygen from the carbonates of sedimentary origin during reaction. The calculated δD of water in equilibrium with the tremolite is around -20 ‰ (Fig. 11), which is lower than the typical magmatic fluid composition. However, this value is consistent with a magmatic fluid being in equilibrium with intrusive rocks at lower temperatures (Fig. 11). Water in equilibrium with the epidote-quartz veins has a $\delta^{18}O$ value around 8 ‰ (Fig. 12a), which is also higher than the estimated magmatic fluid composition at the vein formation temperatures, also indicating some contribution of oxygen from the carbonates. The fluid composition and formation temperatures of the tremolite and epidote-quartz veins are comparable (Figs. 10 and 12a); these similarities suggest that these two vein types may have equilibrated about the same time, with the same fluid, and thus form a conjugate vein system. Carbon dioxide in equilibrium with the forsterite and tremolite veins has higher $\delta^{13}C$ values than typical for magmatic fluid compositions (Fig. 12b). This is not surprising, as there is much less carbon provided from the magmatic fluids, and hence the higher $\delta^{13}C$ CO_2 released from decarbonation reactions of the dolomites is a dominant component of the vein carbon.

In comparison with the forsterite and tremolite veins, the isotopic composition of the fluid calculated for the talc-H_2O pair at the estimated formation temperature is different, with a $\delta^{18}O$ of 0 ‰ and δD of -40 ‰. As mentioned above, water in equilibrium with the tonalites also evolves towards higher δD and lower $\delta^{18}O$ values at 140°C, but there is a deviation of the

calculated water in equilibrium with the talc veins from a typical igneous water trend (Fig. 11). Small uncertainties in these calculations can arise from the use of the fractionation factors at such low temperatures. The initial δD for the magmatic water is also not that well constrained and the chosen value here may be too high. However, fitting the igneous water trend through the calculated value for water in equilibrium with the talc vein would require δD values that are lower than the values typical for primary magmatic water (after Sheppard, 1986). We suggest, then, a mixed fluid of igneous and surface-derived water for the formation of the talc veins. The low formation temperature of the talc-calcite veins would require them to be part of the exhumation history, which agrees well with a change in the regional stress field observed for the talc veins (Fig. 4a). Hence, it is plausible that during the uplift, pathways for infiltration of meteoric fluids could have been created in association with this change of the stress field.

Isotope Exchange Mechanism

The dominant transport mechanism in metasomatic rocks can be deduced with at least two stable isotope systems and a good spatial distribution of the analyses across an isotopic front or reaction progress (Baumgartner & Rumble III, 1988; Baumgartner & Valley, 2001). In simple terms, the shape and position of the stable isotope profile can be used to distinguish between diffusion and infiltration controlling the mass transfer mechanism (Korzhinskii, 1968; Baumgartner & Rumble III, 1988).

The isotopic profiles across the Bergell veins exhibit three characteristic features (Fig. 8 and 9), with (1) the relatively homogenous $\delta^{18}O$ and $\delta^{13}C$ distribution within the replacement and central zones. Some variability of the isotopic composition in the replacement zone can be explained by the presence of minor amounts of dolomite, as the fractionation between dolomite and calcite, at the estimated temperature range, can be up to a

few per mil for the oxygen and carbon isotopes (Northrop & Clayton, 1966; O'Neil & Epstein, 1966; Sheppard & Schwarcz, 1970); (2) the sharp, almost kink-step like O and C isotope fronts; and (3) the spatial coincidence of the $\delta^{18}O$, the $\delta^{13}C$, and mineralogical fronts. As suggested by Taylor & Bucher-Nurminen (1986), the veins are predominantly the result of infiltration of a fluid normal to the central zone, which would be in agreement with the sharp isotopic front in the profiles (e.g. Baumgartner & Rumble III, 1988). However, there are some intriguing consequences regarding the position of the carbon isotopic front relative to that for oxygen. The advancement of the C and O isotope fronts depends on the relative abundance of carbon and oxygen within the fluid and the host-rock (Gerdes *et al.*, 1995). The spatially coincident fronts (e.g. Figs. 8 and 9) would imply that they advance at equal speed, hence that there is an equal amount of carbon and oxygen in the fluid and the carbonates. This is only possible if the binary fluid has an X_{CO2} of 0.5 (i.e. carbon/oxygen concentration ratio of 1/3, same as in the carbonate structure). This fluid composition is very unlikely, as a magmatic fluid originating from volatile exsolution upon cooling of the tonalites would have a very low CO_2 content (e.g. Lowenstern, 2001; Moore, 2008). This is corroborated by phase petrology requiring an $X_{CO2} < 0.1$ to produce the observed mineral assemblages (see following section and Bucher-Nurminen 1981). In a fluid with low CO_2 content, the predicted carbon/oxygen concentration ratio of the infiltrating fluid is very small. In addition, $\delta^{18}O$ and $\delta^{13}C$ of the infiltrating fluid will have much lower (magmatic) values when compared to the dolomites (original sediment). Simple mass balance constraints therefore predict an oxygen isotopic front that advances significantly faster, and a carbon isotopic front that lags behind the oxygen front. This difference is not observed for the Bergell veins (e.g. Fig. 8 and 9). Furthermore, both isotopic fronts coincide with the mineralogical replacement front. That being said, we observe for the forsterite veins that the values measured at the isotopic fronts plot slightly above the mixing line (Fig. 7). This cannot be associated with diffusion as the

shape of the curve is not correct, and it would be indicative of fluids having a much higher

X_{CO2} (Baumgartner and Rumble III, 1988) than what is required for the formation of the

forsterite veins.

The results shown here, thus, indicate that there needs to be an additional, so far,

unrecognized mechanism, to explain the distribution of stable isotopes across these fronts. We

propose that the metamorphic reaction itself is governing the stable isotope exchange of

oxygen and carbon (that is no reaction, no isotopic exchange). The positions of the isotopic

fronts will then be determined by how chemically reactive the fluid is. To get a better

comprehension of the stable isotope exchange mechanism and how it relates to fluid

infiltration and diffusion, further exploration at the grain scale, looking at in-situ stable

isotope distribution, is required (e.g. Bowman et al., 2009; Ferry et al., 2010). Such work has

been done on very similar olivine and calcite veins at the contact with the Adamello intrusion,

and results confirm that even at the grain scale, stable isotopic exchange only occurs through

dissolution – reprecipitation reactions (Bégué *et al.*, 2019). A coupled oxygen isotope

exchange with the reaction has been shown for example by Labotka et al. (2004) in feldspar

reprecipitation experiments, and there are examples showing radiogenic isotopic resetting

related to dissolution-reprecipitation reactions (e.g. Di Vincenzo *et al.*, 2001; Halama *et al.*,

2018).

Formation Reactions of the Vein Mineral Assemblage

The compositional space of the minerals forming the reaction veins can be described

in a five-component system (CaO-MgO-SiO_2-CO_2-H_2O). A T-X_{CO2} phase diagram (Fig. 13a)

was calculated using PerpleX for a constant pressure of 0.3 GPa (Connolly, 1990), revealing

that the temperature ranges for the respective stability fields for forsterite, tremolite and talc

are coherent with the equilibrium temperatures constrained by the oxygen isotope

compositions. Low X_{CO2} values are required, consistent with the predominantly magmatic origin of the fluids. The isochemical T-X_{CO2} phase diagram illustrates the stability fields for the forsterite and tremolite formation (i.e. Fig. 13a) and provides the temperature and X_{CO2} ranges required for the presence of these phases in the assemblages. However, for metasomatic systems, chemical elements are added and/or removed from the system, thus controlling their activity. The silica activity in particular is of major importance in governing the resulting phase assemblage and thus the sequence of reaction zones. In Figure 13a (inset), for instance, quartz is stable with tremolite and dolomite, while it is lacking in the tremolite vein mineral assemblage. There is also no reaction that transforms dolomite into forsterite directly in quartz bearing systems, as is observed in the Bergell veins. Chemical potential diagrams can help explain this discrepancy by reduced quartz activities, as exemplified with the $\mu(SiO_2)$ versus X_{CO2} diagrams (Fig. 13b and c). For the pressure and temperature conditions of the forsterite vein formation (Fig. 13b), forsterite is stable at $\mu(SiO_2)$ values below quartz saturation. The original host rock assemblage (dolomite + calcite) will become unstable in favour of the vein mineral assemblage (forsterite + calcite) by either increasing $\mu(SiO_2)$ or decreasing X_{CO2}, at silica undersaturated conditions. A similar diagram is obtained for the tremolite vein forming conditions (Fig. 13c), with the destabilisation of the dolomite + calcite host assemblage to form tremolite + calcite at $\mu(SiO_2)$ values below quartz saturation, thus not requiring quartz to be stable in the mineral assemblage.

To form either the forsterite-calcite, or tremolite-calcite veins, a set of reactions can be used, starting with the breakdown reaction of the dolomite:

$$CaMg(CO_3)_2 \rightarrow MgO^{fluid} + CaO^{fluid} + 2\ CO_2 \qquad (1)$$

This break-down reaction of dolomite is driven by the infiltration of water and aqueous silica. From (1), calcium, magnesium and CO_2 are available to react with $SiO_2(aq)$ and H_2O to form silicates and calcite within the reaction veins:

$$2\ MgO^{fluid} + SiO_2{}^{fluid} \rightarrow Mg_2SiO_4 \qquad (2)$$

$$5\ MgO^{fluid} + 2\ CaO^{fluid} + 8\ SiO_2{}^{fluid} + H_2O \rightarrow Ca_2Mg_5Si_8O_{22}(OH)_2 \qquad (3)$$

$$CaO^{fluid} + CO_2 \rightarrow CaCO_3 \qquad (4)$$
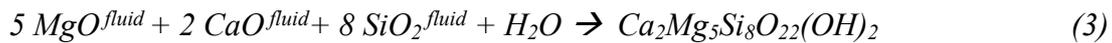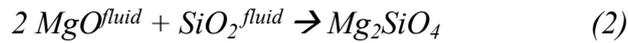
Aqueous metal complexes should ideally be used in the above equations to accurately reflect the metal species transport. However, speciation and solubility in CO_2-bearing fluids are not very well known, and using actual species would not significantly contribute to the understanding of the reaction at the level investigated here (e.g. Pokrovski *et al.*, 2013). Hence, to avoid complicating these reactions, we do not take any speciation of the elements into account. These reactions are written to highlight the fact that dolomite breaks down (reaction 1), while calcite and the silicates are precipitated (reactions 2-4). The reaction progress can be variable in this open system: the amount of dolomite breakdown versus forsterite crystallisation is not directly linked, for example, as there may be some addition of Mg from the intrusion. Similarly, calcite precipitation will depend on how much Ca is added or subtracted by the fluid. Macroscopically, no significant volume change has been observed, as exemplified by the presence of original sedimentary banding that can be followed across the entire replacement zone up to the central fracture and the lack of deformation of these bands, other than a slight shearing component present in some veins (Fig. 5a and d). The presence of calcite in the epidote-quartz veins and endoskarns, and the influence of the sediments in the stable isotope composition of the minerals in the vein (Fig. 12), indicate that the transport of element was bidirectional, and at least some CaO and CO_2 had to be transported from the xenolith to the tonalites. Diffusive mass transport is driven by gradients in chemical potential. As calcite is saturated everywhere in the veins forming in the carbonates (replacement and central zone), CaO would not be able to diffuse, at constant fluid composition. From textural observations, however, calcite in the quartz-epidote veins and endoskarns within the tonalites is either interstitial (e.g. Fig. 2f), or present in small veinlets.

This suggests that this calcite may have formed at a different time and/or temperature compared to the calcite in the carbonate veins, which would then not impede calcium transport towards the intrusion.

Formation Mechanism of the Veins

The metasomatic forsterite and tremolite veins are shown to have been externally buffered by magmatic fluids. Likewise, field geometry and the mineral reactions proposed to form the forsterite and tremolite veins, imply mass transport of SiO_2 and H_2O from the intrusion into the carbonates, countered by a net flux of CaO and CO_2 from the carbonates towards the intrusion (e.g. Figs. 2d and 14). This raises interesting questions not only regarding the fluids necessary for their formation, but also about the mechanical processes associated with this fracture-focused fluid infiltration.

The orientation of these fractures is controlled by the regional stress field, which changes prior to the talc vein formation event (Fig. 4). This type of extensional failure is commonly associated with hydrofracturing normal to the minimal stress σ_3 (e.g. Secor, 1965; Phillips, 1972; Cox et al., 1987; Cosgrove, 1995; Sibson, 2000; and reviews by Oliver, 1996; Bons et al., 2012). It occurs when the fluid pressure exceeds σ_3 plus the tensile strengths ($P_f > \sigma_3 + T$; e.g. Secor, 1965; Etheridge, 1983). In a Mohr-Griffith-Coulomb failure diagram, this would result in a Mohr circle intersecting the failure envelope at its leftmost side (that is, the smallest normal stress, Fig. 14 a; e.g. Phillips, 1972; Cosgrove, 1995). At high confining pressures, pure extension fracture can only occur at elevated fluid pressure conditions (shifting the Mohr circle to the left; Secor, 1965; Phillips, 1972; Cox et al., 1987; Cosgrove, 1995), which is the trigger to fracturing (Fig. 14a). Gradients in the hydraulic head will then cause the fluid to be pumped through the rock, and fracturing stops once stress levels below critical hydrofracturing pressure are reached.

This is a compelling mechanism to explain the Bergell veins, as one of their particularities is that they are not "through-going" (that is they are initiated at the contact and end within the xenolith, a few meters from the contact; as shown schematically in Fig. 14b). While some veins have only one type of bi-mineral reaction zone (e.g. the veins studied in more detail here), others are more complex, indicating a succession of reaction zones (Bucher-Nurminen, 1981), and hence, a succession of hydrofracturing and fluid infiltration pulses. Similarly, some of the tremolite veins have been completely replaced by late talc, while others were spared from this replacement. We suggest that these more complex veins (Fig. 3), and the replaced tremolite veins, are associated with repeated failure along the same fracture due to an incomplete seal or an inherited weakness (that is, no cohesion compared to the surrounding carbonates). Yet, if the seal is efficient enough to completely recover cohesion, these veins may be much more difficult to crack again and new fractures will form elsewhere (e.g. Bons et al. 2012), leaving the previously formed reaction zone and vein almost unchanged. Due to the perfect symmetry of the complex veins (e.g. Bucher-Nurminen, 1981), the re-fracturing had to occur at or close to the vein centre. The original fracturing occurred through intermittently elevated fluid pressures (e.g. Fig. 14a), and the observations that the veining initiated from the contact and propagated at right angles into the carbonates and the tonalites, suggests that the fluid build-up had to occur at the contact zones. Based on our observations, we suggest the following geometry for the xenolith/intrusion relationship: the studied outcrops represent a fully enclosed carbonate xenolith surrounded by intrusive rock, following the general flattening type of strain, due to a $\sigma1$ stress field in a SSE-NNW direction, oriented perpendicularly to the contacts (Fig. 14b). This stress field also explains the orientation of the veins in the carbonates. Elevated fluid pressures, in excess of the confining pressures related to the regional and intrusion emplacement stress field, were responsible for the initial fracturing of the carbonates and intrusive rocks. Contact zones

between the tonalites and carbonates have served as fluid conduits, where dominantly igneous fluids accumulated and the pressure built up until hydrofracturing occurred. The observed contact skarns present the most complex mineralogy, with important alteration and overprinting of the original mineral assemblages, indicating a long-lived, fluid-mediated formation at variable temperatures. These fluids contained the dissolved elements needed to form the reaction zones, in agreement with the fact that SiO_2, FeO and H_2O have to be externally provided to the carbonates. Similarly, to crystallise calcite in the epidote-quartz veins and the endoskarns, CaO and CO_2 are transported towards the intrusion (Fig. 14c).

Important implications regarding "fluid flow" systems result from this mechanism. If fluid infiltration is limited to episodic fracturing of the carbonates and the tonalites, it will cease when the fracturing stops. This implies that fluids are not continuously flushing through the system to form the reaction. Infiltration of episodic pulses of highly reactive fluid are therefore suggested for the formation of these veins. The veins would have "opened" very rapidly on fracturing, and the associated fluid, once infiltrated, would have remained stationary in the entire fracture at pressure σ_3. The absence of any gradients in stable isotope values or differences in across-vein profiles along the vein (e.g. between the centre and the ends of the tremolite vein; Fig. 5b and Table 1) also support this mechanism. With time, the fracture seals, and fluid leaves the rock, most likely in a pervasive manner not recorded by geochemistry nor structure, possibly because the fluid pressure is not high enough anymore to sustain an "open" vein. Tracing fluid movements is only possible if the fluid reacts with its surroundings; therefore, no specific reactions can be identified to be related to fluid withdrawn because the fluid had lost its chemical reactivity. To form a new reaction vein or zone, new and low X_{CO2} fluids would have to infiltrate the system along a new or an existing fracture (for example to form the tremolite reaction zones after the forsterite ones, or the iron enrichment during the development of the tremolite reaction zones; Figs. 3 and 6).

32

How Much Fluid is Needed to Generate the Reaction Zones?

We suggest that the dolomite protolith fractures due to elevated fluid pressure at the

contact zones, allowing for fluids to infiltrate the fracture and react with the host rock. The

fluids do not flush through the system; fluids are limited to the contact skarn environments

and the veins. The fluids remain present in the fractures and in the contact skarn zones, acting

as "highways" for the transport of elements between xenolith and intrusive rocks. This system

- the xenolith and the surrounding tonalites - can be approximated by a closed system (i.e.

Fig. 14b).

With this model in mind we can proceed to calculate the minimum amount of

intrusive rock within the system that would be required to supply the water necessary to

produce the metasomatic reaction veins at $X_{CO2} = 0.05$, the maximum value allowed by

isotope thermometry and phase equilibria for the forsterite + calcite veins, or at $X_{CO2} = 0.01$

for the tremolite + calcite veins (Fig. 13). To simplify our calculations, we consider a pure

dolomitic xenolith of 10 m^3. For a typical xenolith about 10 vol.% is reacted to form the

veins, or hence a volume of 1 m^3 (with remaining 9 m^3 of unreacted dolomite). The volume of

intrusive rocks required to transform this 1 m^3 of dolomite into either forsterite + calcite, or

tremolite + calcite can be calculated, assuming that the fluids are all magmatically derived. A

set of equations has been established to calculate the evolution of fluid composition as a

function of reaction progress or vice-versa to evaluate the degree of which mineral

assemblages can control or be buffered by the composition of a coexisting fluid (Ferry, 1980;

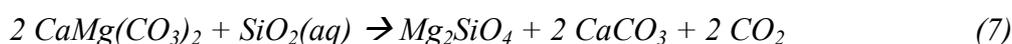Rice & Ferry, 1982; modified after Greenwood, 1975):

$$X_{CO2} = \frac{(n_{CO2})}{\left(n_{H2O}^0 + n_{CO2}^0\right) + A(n_{CO2} + n_{CO2}^0)} \qquad \text{with} \quad A = \frac{v_{H2O} + v_{CO2}}{v_{CO2}} \qquad (5)$$

Here, n_{H2O} and n_{CO2} are the number of moles of H$_2$O and CO$_2$ in the fluid, whereas the

superscript ^{0} denotes the initial conditions. v_{H2O} and v_{CO2} are the stoichiometric coefficients

of H_2O and CO_2 in the reaction of interest. This equation can be re-written to calculate the

amount of initial fluid needed, assuming that the igneous fluid is pure H_2O. Hence equation

(5) can be simplified to:

$$n_{H2O}^{inf} = \frac{n_{CO2}}{X_{CO2}} - A\, n_{CO2} \qquad (6)$$

with n_{H2O}^{inf} representing the number of moles of H_2O needed to infiltrate the vein to maintain a

low X_{CO2} fluid. For these calculations, we assume a closed system, and rewrite the forsterite

and tremolite forming reactions by combining reactions (1) to (4):

$2\ CaMg(CO_3)_2 + SiO_2(aq) \rightarrow Mg_2SiO_4 + 2\ CaCO_3 + 2\ CO_2$ *(7)*

$5\ CaMg(CO_3)_2 + 8\ SiO_2(aq) + H_2O \rightarrow Ca_2Mg_5Si_8O_{22}(OH)_2 + 3\ CaCO_3 + 7\ CO_2$ *(8)*

For the forsterite reaction (7), it can be seen that each mole of dolomite produces 1

mole of CO_2, and, using the molar volumes (Table 4; Pitzer and Sterner, 1994), 1 m^3 of

dolomite would produce 0.8 m^3 of CO_2 (Table 4). To preserve an X_{CO2} of 0.05 (Fig. 13),

transformation of the initial 1 m^3 of dolomite would require introduction of 7 m^3 of pure H_2O

into the reacting dolomite marble (Table 4). Applying similar calculations to reaction (8), i.e.

for the tremolite vein at lower X_{CO2} (0.01; Fig. 13) and considering additional minor structural

water that is required, 1.0 m^3 of CO_2 is produced. This amount requires about 45 m^3 of H_2O to

maintain X_{CO2} at 0.01 (Table 4). Note that these results are not comparable to the large

amounts of fluids calculated by Ferry (1995) for the ophicarbonates further south in the

Bergell contact aureole. In their study, the fluid is derived from dehydration reactions of the

serpentinite host rock during prograde metamorphism, and do not reflect infiltration of

externally derived fluids as is the case for the metasomatic veins studied here.

We can now estimate how much intrusive rock would be necessary to provide these

volumes of fluids. At 0.3 GPa, a magma of tonalitic composition would have ~6 wt.% H_2O at

water saturation (e.g. Moore, 2008), yet the subsolidus intrusive rock is almost dry, except for

a small fraction of fluid left as structural water in minerals and negligible fluid/melt

inclusions. If we assume that the magma exsolved about 5 wt.% fluid upon cooling and crystallisation, 1 m^3 of intrusive rock, with a density of about 2.7×10^6 g/m^3, would produce 7.5×10^3 mol of fluid. For the formation temperatures of the forsterite and tremolite vein, this corresponds to 0.19 m^3 and 0.16 m^3 of fluid, respectively. Hence, to transform 1 m^3 of dolomite into forsterite + calcite, about 40 m^3 of intrusive rock would be required to obtain a final a X_{CO2} of 0.05; for the tremolite + calcite reaction, with a X_{CO2} of 0.01, 290 m^3 of intrusion is necessary (Table 4). These results imply that the closed system can be described by a volumetric intrusive to carbonate rock ratio of 4:1 for the forsterite + calcite reaction, and 30:1 for the tremolite + calcite vein formation, respectively. The volumetric amounts of xenoliths in the Bergell tonalite is relatively small, and hence these proportions are easily available. Note that, if the initial water concentration of the tonalite is lower than estimated here, larger intrusive to xenolith ratios would be required. Nonetheless, these calculations show that the resulting amount of water needed to explain the observed features is not excessively large and could likely be "locally" provided by the intrusive rocks cooling and crystallizing around the xenoliths.

The model of Taylor & Bucher (1986) is based on a flow-through system. To constrain the amount of fluids necessary to form the veins, they calculated the amount of silica that can be dissolved in a pure H_2O fluid at a given temperature, based on quartz solubility (Fournier & Potter, 1982), and the amount of silica needed to react with the dolomites to produce the new silicate minerals. They assume that silica is stripped from the fluid in a one-pass fluid-flushing model. Consequently, a larger amount of fluid corresponding to a larger volume of intrusion would be required to provide the necessary SiO_2(aq). A similar model has been calculated using the SiO_2 solubility model from Manning (1994), resulting in required water amounts that are 10, respectively 15 times larger for the forsterite and tremolite veins compared to the X_{CO2} conservation approach (Table 4).

Considering that the silica molality decreases with increasing X_{CO2} (Walther & Orville, 1983) and that the mineral assemblages in the veins formed at quartz-undersaturated conditions, these calculated volumes are likely underestimated if we were to use fluid compositions dictated by phase petrology. But, given the field observations, where most of the carbonate "inclusions" are true xenoliths without any connection to the sediments in the contact aureole and the vein endings are recognizable (Fig. 14b), a continuous fluid flow is prevented. Thus, using one-pass fluid-flushing as hypothesis to calculate required fluid volumes is not an adequate model to start out with (Taylor & Bucher-Nurminen, 1986; Bucher-Nurminen, 1989).

Fluid flushing is not required in our model; silica transport to supply the necessary SiO_2 to the veins is suggested to occur through diffusion in the stationary fluid (Fig. 14c). Experiments by Ildefonse & Gabis (1976) and Watson & Wark (1997) show that Si diffusion in stationary fluids is highly effective. At formation temperatures for the forsterite (555 °C) and tremolite (390°C) veins, for instance, silica would diffuse over 65 cm and 25 cm in one year, respectively, in quartz-saturated water (using diffusion coefficient of Watson & Wark, 1997). In an open-vein system, transport will not be hindered by porosity (Fig. 14c). Given this rapid diffusion of silica (and other elements, see Oelkers and Helgeson, 1988) in a fluid phase, it is reasonable to assume that silica and other cations show little gradient throughout the central vein zone, and hence, they are easily accessible for the formation of the vein minerals. Thus, silica availability is not a limiting factor in those metasomatic exchange reactions.

To summarize, we propose a formation model requiring only relatively small amounts of fluids that infiltrated the veins through episodic events along hydrofractures during the cooling history of the intrusion. This fluid remained stationary within these veins, at least as long as the reaction with the host-rock occurred, rather than flushing through the central

fracture. Smaller fluid volumes would also be more easily absorbed by the surrounding intrusive rocks, as, except for the epidote-quartz veins, no major fluid movements are evident from field observations within the tonalites. We note that similar veins have not been observed elsewhere around the Bergell either, pointing to the fact that this vein formation may only be a localized event. This localized occurrence, restricted size (length) of these veins, and the lack of evidence of large-scale fluid movement in the tonalites argue that there is no need to involve a larger convective hydrothermal system.

CONCLUSIONS

New stable isotope data on carbonates and silicates have been combined with phase petrology and field observations to re-evaluate the formation mechanism of metasomatic reaction veins in dolomitic xenoliths in the Bergell tonalites. The study of multiple generations of veins and the calculations of equilibrium temperatures from distinct mineral pairs confirmed their formation along a retrograde cooling path. The following can be deduced from this work:

(1) The stable isotope data indicate that the veins are buffered by fluids originating from the intrusion. The late and low temperature talc veins may have formed under different conditions involving a mixture of magmatic and meteoric water.

(2) The $\delta^{18}O$ and $\delta^{13}C$ profiles across veins are flat and coincide exactly with the sharp mineralogical front between the veins and the unchanged dolomites. These results indicate a mechanism of coupled isotopic and chemical exchange, which is related to the dissolution and re-precipitation reactions producing the metasomatic reaction veins.

(3) Hydrofracturing occurs due to increased fluid pressure at the contact zones between the dolomites and the tonalite, which are suggested to serve as fluid conduits. The

fracturing stops once the pressure decreases below critical levels. We suggest that the veins formed through episodic pulses of highly reactive fluids which remained stationary within these veins for at least as long as the reaction with the host-rock occurred, rather than flushing through the central fracture.

(4) Considering an X_{CO2} - constrained mass balance, the formation of the veins would only require a relatively small amount of fluid, which could theoretically all be released from the intrusive rocks in vicinity of the xenoliths.

(5) Veining is not ubiquitous around the Bergell intrusion, indicating that vein formation may have been a localized event. There is no need to involve a larger convective hydrothermal system.

REFERENCES

Baker, T., Van Achterberg, E., Ryan, C. G. & Lang, J. R. (2004). Composition and evolution of ore fluids in a magmatic-hydrothermal skarn deposit. *Geology* **32**, 117–120.

Baumgartner, L. P. & Rumble III, D. (1988). Transport, Transport of stable isotopes: I: Development of a kinetic continuum theory for stable isotope. *Contributions to Mineralogy and Petrology* **98**, 417–430.

Baumgartner, L. P. & Valley, J. W. (2001). Stable isotope transport and contact metamorphic fluid flow. *Reviews in Mineralogy and Geochemistry*. Mineral Soc America **43**, 415–467.

Bégué, F., Baumgartner, L., Bouvier, A.-S., Putlitz, B. & Vennemann, T. (2016). Reactive fluid-flow and stable isotope exchange related to hydrothermal veins in carbonate xenoliths: A coupled CL imaging and SIMS study. *Geological Society of America Abstracts with Programs*.

Bégué, F., Baumgartner, L. P., Bouvier, A.-S. & Robyr, M. (2019). Reactive fluid infiltration along fractures: Textural observations coupled to in-situ isotopic analyses. *Earth and Planetary Science Letters* **519**, 264–273.

Berger, A. & Gieré, R. (1995). Structural observations at the eastern contact of the Bergell Pluton. *Schweizerische Mineralogische und Petrographische Mitteilungen*. St{ä}ubli **75**, 241–258.

Berger, A., Rosenberg, C. L. & Schmid, S. M. (1996). Ascent, emplacement and exhumation of the Bergell pluton within the Southern Steep Belt of the Central Alps. *Schweizer Mineralogische Petrographische Mitteilungen*. St{ä}ubli **26**, 357–382.

Berman, R. G. (1988). Internally-Consistent Thermodynamic Data for Minerals in the System Na2O-K2O-CaO-MgO-FeO-Fe2O3-Al2O3-SiO2- TiO2-H2O-CO2. *Journal of Petrology* **29**, 445–522.

Bons, P. D., Elburg, M. A. & Gomez-Rivas, E. (2012). A review of the formation of tectonic veins and their microstructures. *Journal of Structural Geology*. Elsevier Ltd **43**, 33–62.

Bowman, J. R., Valley, J. W. & Kita, N. T. (2009). Mechanisms of oxygen isotopic exchange and isotopic evolution of 18O/16O-depleted periclase zone marbles in the Alta aureole, Utah: Insights from ion microprobe analysis of calcite. *Contributions to Mineralogy and Petrology* **157**, 77–93.

Bowman, J. R., Willett, S. D. & Cook, S. J. (1994). Oxygen isotopic transport and exchange during fluid flow: one-dimensional models and applications. *American Journal of Science* **294**, 1–55.

Bucher-Nurminen, K. (1981). The formation of metasomatic reaction veins in dolomitic marble roof pendants in the Bergell intrusion (Province Sondrio, northern Italy). *American Journal of Science* **281**, 1197–1222.

Bucher-Nurminen, K. (1987). The composition of hydrothermal fluids responsible for silicate reaction veins in dolomitic marbles. *Chemical Transport in Metasomatic Processes* 759–762.

Bucher-Nurminen, K. (1989). Reaction veins in marbles formed by a fracture-reaction-seal mechanism. *European Journal Mineralogy* **1**, **701–714**, 1989.

Bucher, K. (1998). Growth mechanisms of metasomatic reaction veins in dolomite marbles from the Bergell Alps. *Mineralogy and Petrology* **63**, 151–171.

Burkhard, M. & Kerrich, R. (1988). Fluid regimes in the deformation of the Helvetic nappes, Switzerland, as inferred from stable isotope data. *Contributions to Mineralogy and Petrology* **99**, 416–429.

Cartwright, I., Power, W. L., Oliver, N. H. S., Valenta, R. K. & Mclatchie, G. S. (1994). Fluid migration and vein formation during deformation and greenschist facies metamorphism at Ormiston Gorge, central Australia. *Journal of Metamorphic Geology*. Blackwell

Publishing Ltd **12**, 373–386.

Cartwright, I., Vry, J. & Sandiford, M. (1995). Changes in stable isotope ratios of metapelites and marbles during regional metamorphism, Mount Lofty Ranges, South Australia: implications for crustal scale fluid flow. *Contributions to Mineralogy and Petrology* **120**, 292–310.

Chacko, T., Cole, D. R. & Horita, J. (2001). Equilibrium Oxygen, Hydrogen and Carbon Isotope Fractionation Factors Applicable to Geologic Systems. *Reviews in Mineralogy and Geochemistry* **43**, 1–81.

Chiba, H., Chacko, T., Clayton, R. N. & Goldsmith, J. R. (1989). Oxygen isotope fractionation involving diopside, forsterite, magnetite, and calcite: Application to geothermometry. *Geochimica et Cosmochimica Acta* **53**, 2985–2995.

Clayton, R. N. & Epstein, S. (1961). The Use of Oxygen Isotopes in High-Temperature Geological Thermometry. *The Journal of Geology* **69**, 447–452.

Connolly, J. A. D. (1990). Multivariable phase diagrams: an algorithm based on generalized thermodynamics. *American Journal of Science* **290**, 666–718.

Coplen, T. B., Kendall, C. & Hopple, J. (1983). Comparison of stable isotope reference samples. *Nature* **302**, 236–238.

Cosgrove, J. W. (1995). The expression of hydraulic fracturing in rocks and sediments. *Geological Society, London, Special Publications* **92**, 187–196.

Cox, S. F., Etheridge, M. A. & Wall, V. J. (1987). The role of fluids in syntectonic mass transport, and the localization of metamorphic vein-type ore deposists. *Ore Geology Reviews*. Elsevier **2**, 65–86.

Craig, H. (1957). Isotopic standards for carbon and oxygen and correction factors for mass spectrometric analyses of carbon dioxide. *Geochimica Cosmochimica Acta*, 133–149.

Craig, H. (1961). Isotopic Variations in Meteoric Waters. *Science (New York, N.Y.)* **133**,

1702–1703.

Davidson, C., Rosenberg, C. & Schmid, S. M. (1996). Synmagmatic folding of the base of the Bergell pluton, Central Alps. *Tectonophysics* **265**, 213–238.

Di Vincenzo, G., Ghiribelli, B., Giorgetti, G. & Palmeri, R. (2001). Evidence of a close link between petrology and isotope records : constraints from SEM, EMP, TEM and in situ 40Ar-39Ar laser analyses on multiple generations of white micas (Lanterman Range, Antarctica). *Earth and Planetary Science Letters* **192**, 389–405.

Durand, C., Boulvais, P., Marquer, D. & Rossy, M. (2006). Stable isotope transfer in open and closed system across chemically contrasted boundaries: Metacarbonate - Granitoid contacts in the Quérigut magmatic complex (Eastern Pyrenees, France). *Journal of the Geological Society* **163**, 827–836.

Eiler, J. M., Valley, J. W. & Baumgartner, L. P. (1993). A new look at stable isotope thermometry. *Geochimica et Cosmochimica Acta* **57**, 2571–2583.

Einaudi, M. T. & Burt, D. M. (1982). A special issue devoted to skarn deposits: Introduction - Terminology, Classification, and Composition of skarn deposits. *Economic Geology* **77**, 745–754.

Einaudi, M. T., Meinert, L. D. & Newberry, R. J. (1981). Skarn deposits. In: Skinner & B.J. (eds) *Economic Geology seventy-fifth anniversary volume*, 317–391.

Etheridge, M. A. (1983). Differential stress magnitudes during regional deformation and metamorphism: upper bound imposed by tensile fracturing. *Geology*, 231–234.

Ferry, J. M. (1980). A case study of the amount and distribution of heat and fluid during metamorphism. *Contrib. Mineral. Petrol.* **71**, 373–385.

Ferry, J. M. (1986). Reaction Progress: A Monitor of Fluid Rock Interaction During Metamorphic and Hydrothermal Events. *Water-Rock Interactions During Metamorphism. Advances in Physical Gechemistry* **5**, 61–88.

Ferry, J. M. (1992). Regional metamorphism of the waits river formation, Eastern Vermont: Delineation of a new type of giant metamorphic hydrothermal system. *Journal of Petrology* **33**, 45–94.

Ferry, J. M. (1995). Fluid flow during contact metamorphism of ophicarbonate rocks in the Bergell aureole, Val Malenco, Italian Alps. *Journal of Petrology*. Oxford University Press **36**, 1039–1053.

Ferry, J. M., Ushikubo, T., Kita, N. T. & Valley, J. W. (2010). Assessment of grain-scale homogeneity and equilibration of carbon and oxygen isotope compositions of minerals in carbonate-bearing metamorphic rocks by ion microprobe. *Geochimica et Cosmochimica Acta*. Elsevier Ltd **74**, 6517–6540.

Ferry, J. M., Ushikubo, T. & Valley, A. W. (2011). Formation of forsterite by silicification of dolomite during contact metamorphism. *Journal of Petrology* **52**, 1619–1640.

Ferry, J. M., Wing, B. A., Penniston-Dorland, S. C. & Rumble, D. (2001). The direction of fluid flow during contact metamorphism of siliceous carbonate rocks: new data for the Monzoni and Predazzo aureoles, northern Italy, and a global review. *Contributions to Mineralogy and Petrology* **142**, 679–699.

Fournier, R. O. & Potter, R. W. (1982). An equation correlating the solubility of quartz in water from 25° to 900°C at pressures up to 10,000 bars. *Geochimica et Cosmochimica Acta* **46**, 1969–1973.

Friedman, I. & O'Neil, J. R. (1977). *Data of geochemistry: Compilation of stable isotope fractionation factors of geochemical interest*. US Government Printing Office.

Gerdes, M., Baumgartner, L. & Valley, J. (1999). Stable Isotopic Evidence for Limited Fluid Flow through Dolomitic Marble in the Adamello Contact Aureole, Cima Uzza, Italy. *Journal of Petrology* **40**, 853–872.

Gerdes, M. L., Baumgartner, L. P., Person, M. & Rumble, D. (1995). One- and 2-

Dimensional Models of Fluid-Flow and Stable-Isotope Exchange At an Outcrop in the Adamello Contact Aureole, Southern Alps, Italy. *American Mineralogist* **80**, 1004–1019.

Gianola, O., Schmidt, M. W., von Quadt, A., Peytcheva, I., Luraschi, P. & Reusser, E. (2014). Continuity in geochemistry and time of the Tertiary Bergell intrusion (Central Alps). *Swiss Journal of Geosciences* **107**, 197–222.

Gieré, R. (1985). Metasedimente der Suretta-Decke am Ost-und Sudostrand der Bergeller Intrusion: Lithostratigraphische Korrelation und Metamorphose. *Schweizerische Mineralogische und Petrographische Mitteilungen*. Leemann **65**, 57–78.

Graham, C. M., Harmon, R. S. & Sheppard, S. M. F. (1984). Experimental hydrogen isotope studies: Hydrogen isotope exchange between amphibole and water. *American Mineralogist* **69**, 128–138.

Greenwood, H. J. (1975). Buffering of pore fluids by metamorphic reactions. *American Journal of Science* **275**, 573–593.

Halama, R., Glodny, J., Konrad-schmolke, M. & Sudo, M. (2018). Rb-Sr and in situ 40 Ar / 39 Ar dating of exhumation-related shearing and fluid-induced recrystallization in the Sesia zone (Western Alps , Italy). *Geosphere* **14**, 1425–1450.

Hermann, J., Rubatto, D. & Trommsdorff, V. (2006). Sub-solidus Oligocene zircon formation in garnet peridotite during fast decompression and fluid infiltration (Duria, Central Alps). *Mineralogy and Petrology* **88**, 181–206.

Holness, M. B. (1997). Fluid flow paths and mechanisms of fluid infiltration in carbonates during contact metamorphism: the Beinn an Dubhaich aureole, Skye. *Journal of Metamorphic Geology* **15**, 59–70.

Hutchison, C. S. (1974). *Laboratory handbook of petrographic techniques*. Wiley-Interscience.

IAEA/WMO (2019). *Global Network of Isotopes in Precipitation. The GNIP Database.*

Accessible at: https://nucleus.iaea.org/wiser. .

Ildefonse, J.-P. & Gabis, V. (1976). Experimental study of silica diffusion during metasomatic reactions in the presence of water at 550°C and 1000 bars. *Geochimica et Cosmochimica Acta* **40**, 297–303.

Jamtveit, B. & Austrheim, H. (2010). Metamorphism: The role of fluids. *Elements* **6**, 153–158.

Jonas, L., John, T., King, H. E., Geisler, T. & Putnis, A. (2014). The role of grain boundaries and transient porosity in rocks as fluid pathways for reaction front propagation. *Earth and Planetary Science Letters* **386**, 64–74.

Jonas, L., Müller, T., Dohmen, R., Immenhauser, A. & Putlitz, B. (2017). Hydrothermal replacement of biogenic and abiogenic aragonite by Mg-carbonates – Relation between textural control on effective element fluxes and resulting carbonate phase. *Geochimica et Cosmochimica Acta*. Pergamon **196**, 289–306.

Kerrick, D. M. & Caldeira, K. (1998). Metamorphic CO2 degassing from orogenic belts. *Chemical Geology*. Elsevier **145**, 213–232.

Kerrick, D. M. & Jacobs, G. K. (1981). A modified Redlich-Kwong equation for H2O, CO2, and H2O-CO2 mixtures at elevated pressures and temperatures. *American Journal of Science*. Kline Geology Laboratory, Yale University **81**, 735–767.

Korzhinskii, D. S. (1968). The theory of metasomatic zoning. *Mineralium Deposita* **3**, 222–231.

Labotka, T. C., Cole, D. R., Riciputi, L. R. & Fayek, M. (2004). Diffusion of C and O in calcite from 0.1 to 200 MPa. *American Mineralogist* **89**, 799–806.

Lacroix, B. & Vennemann, T. (2015). Empirical calibration of the oxygen isotope fractionation between quartz and Fe-Mg-chlorite. *Geochimica et Cosmochimica Acta*. Pergamon **149**, 21–31.

Ligang, Z., Jingxiu, L. I. U., Huanbo, Z. & Zhensheng, C. (1989). Oxygen isotope fractionation in the quartz-water-salt system. *Economic Geology* **84**, 1643–1650.

Lowenstern, J. B. (2001). Carbon dioxide in magmas and implications for hydrothermal systems. *Mineralium Deposita*. Springer **36**, 490–502.

Manning, C. E. (1994). ScienceDirect.com - Geochimica et Cosmochimica Acta - The solubility of quartz in H2O in the lower crust and upper mantle. *Geochimica et Cosmochimica Acta* **58**, 4831–4839.

Matthews, A. & Schliestedt, M. (1984). Evolution of the blueschist and greenschist facies rocks of Sifnos, Cyclades, Greece - A stable isotope study of subduction-related metamorphism. *Contributions to Mineralogy and Petrology* **88**, 150–163.

Meinert, L. D. (1992). Skarns and skarn deposits. *Geoscience Canada* **19**, 145–162.

Moore, G. (2008). Interpreting H2O and CO2 Contents in Melt Inclusions: Constraints from Solubility Experiments and Modeling. *Reviews in Mineralogy and Geochemistry* **69**, 333–362.

Moticska, P. (1970). Petrographie und Strukturanalyse des westlichen Bergeller Massivs und seines Rahmens. .

Müller, T., Baumgartner, L. P., Foster, C. T., Bowman, J. R., Massif, S. A., Baumgartner, L. P., Foster, C. T., Mu, T. & Bowman, J. R. (2009). Crystal size distribution of periclase in contact metamorphic dolomite marbles from the Southern Adamello Massif, Italy. *Journal of Petrology* **50**, 451–465.

Müller, T., Baumgartner, L. P., Foster, C. T., Roselle, G. T., M, T., B, L. P., J, C. T. F. & R, G. T. (2008). Forward modeling of the effects of mixed volatile reaction, volume diffusion, and formation of submicroscopic exsolution lamellae on calcite-dolomite thermometry. *American Mineralogist* **93**, 1245–1259.

Müller, T., Baumgartner, L. P., Foster, C. T. T., Vennemann, T. W. & Mu, T. (2004).

Metastable prograde mineral reactions in contact aureoles. *Geology* **32**, 821.

Müntener, O., Hermann, J. & Trommsdorff, V. (1999). Guidebook for the Excursion to Val Malenco (Eastern Central Alps). .

Nabelek, P. I. (2002). Calc-silicate reactions and bedding-controlled isotopic exchange in the Notch Peak aureole, Utah: Implications for differential fluid fluxes with metamorphic grade. *Journal of Metamorphic Geology* **20**, 429–440.

Nabelek, P. I. (2007). Fluid evolution and kinetics of metamorphic reactions in calc-silicate contact aureoles - From H2O to CO2 and back. *Geology* **35**, 927–930.

Northrop, D. A. & Clayton, R. N. (1966). Oxygen-Isotope Fractionations in Systems Containing Dolomite. *The Journal of Geology* **74**, 174–196.

O'Neil, J. R. & Epstein, S. (1966). Oxygen isotope fractionation in the system dolomite-calcite-carbon dioxide. *Science* **152**, 198–201.

Oelkers, E. H. & Helgeson, H. C. (1988). Calculation of the thermodynamic and transport properties of aqueous species at high pressures and temperatures: Aqueous tracer diffusion coefficients of ions to 1000°C and 5 kb. *Geochimica et Cosmochimica Acta* **52**, 63–85.

Oliver, N. H. S. (1996). Review and classification of structural controls on fluid flow during regional metamorphism. *Journal of Metamorphic Geology*. Blackwell Science Ltd. **14**, 477–492.

Oliver, N. H. S., Cartwright, I., Wall, V. J. & Golding, S. D. (1993). The stable isotope signature of kilometre-scale fracturedominated metamorphic fluid pathways, Mary Kathleen, Australia. *Journal of Metamorphic Geology*. Wiley/Blackwell (10.1111) **11**, 705–720.

Penniston-Dorland, S. C. & Ferry, J. M. (2008). Element mobility and scale of mass transport in the formation of quartz veins during regional metamorphism of the Waits River

Formation , east-central Vermont. *American Mineralogist* **93**, 7–21.

Penniston-Dorland, S. C., Sorensen, S. S., Ash, R. D. & Khadke, S. V. (2010). Lithium isotopes as a tracer of fluids in a subduction zone mélange: Franciscan Complex, CA. *Earth and Planetary Science Letters*. Elsevier B.V. **292**, 181–190.

Person, M. & Baumgartner, L. (1995). New evidence for long-distance fluid migration within the Earth's crust. *Reviews of Geophysics* **33**, 1083–1091.

Phillips, W. J. (1972). Hydraulic fracturing and mineralization. *Journal of the Geological Society* **128**, 337–359.

Pitzer, K. S. & Sterner, S. M. (1994). Equations of state valid continuously from zero to extreme pressures for H2O and CO2. *The Journal of Chemical Physics* **101**, 3111–3116.

Pokrovski, G. S., Borisova, A. Y. & Bychkov, A. Y. (2013). Speciation and Transport of Metals and Metalloids in Geological Vapors. *Reviews in Mineralogy and Geochemistry* **76**, 165–218.

Putnis, A. & Austrheim, H. (2013). Mechanisms of Metasomatism and Metamorphism on the Local Mineral Scale: The Role of Dissolution-Reprecipitation During Mineral Re-equilibration. *Metasomatism and the Chemical Transformation of Rock*. Springer, Berlin, Heidelberg.

Rice, J. M. & Ferry, J. M. (1982). Buffering, infiltration, and the control of intensive variables during metamorphism. *Reviews in Mineralogy and Geochemistry*. Mineral Soc America **10**, 263–326.

Rosenberg, C. L. (2004). Shear zones and magma ascent: A model based on a review of the Tertiary magmatism in the Alps. *Tectonics* **23**.

Rosenberg, C. L., Berger, A. & Schmid, S. M. (1995). Observations from the floor of a granitoid pluton: inferences on the driving force of final emplacement. *Geology*, 443–446.

Rumble, D. (1982). Stable isotope fractionation during metamorphic devolatilization reactions. *Reviews in Mineralogy and Geochemistry* **10**, 327–353.

Rumble, D. & Hoering, T. C. (1994). Analysis of Oxygen and Sulfur Isotope Ratios in Oxide and Sulfide Minerals by Spot Heating with a Carbon Dioxide Laser in a Fluorine Atmosphere. *Ace. Chem. Res.* **27**, 237–241.

Saccocia, P. J., Seewald, J. S. & Shanks, W. C. (2009). Oxygen and hydrogen isotope fractionation in serpentine-water and talc-water systems from 250 to 450 °C, 50 MPa. *Geochimica et Cosmochimica Acta* **73**, 6789–6804.

Samperton, K. M., Schoene, B., Cottle, J. M., Brenhin Keller, C., Crowley, J. L. & Schmitz, M. D. (2015). Magma emplacement, differentiation and cooling in the middle crust: Integrated zircon geochronological-geochemical constraints from the Bergell Intrusion, Central Alps. *Chemical Geology*. Elsevier B.V. **417**, 322–340.

Savin, S. M. & Lee, M. (1988). Isotopic studies of phyllosilicates. In: S.W. Bailey (ed.) *Hydrous Phyllosilicates (Exclusive of Micas)*, 189–223.

Scheele, N. & Hoefs, J. (1992). Carbon isotope fractionation between calcite, graphite and CO2: an experimental study. *Contributions to Mineralogy and Petrology* **112**, 35–45.

Schmid, S. M., Berger, A., Davidson, C., Gieré, R., Hermann, J., Nievergelt, P., Puschnig, A. & Rosenberg, C. L. (1996a). The Bergell pluton (Southern Switzerland, Northern Italy): overview accompanying a geological-tectonic map of the intrusion and surrounding country rocks. *Schweizerische Mineralogische und Petrographische Mitteilungen*. St{ä}ubli **76**, 332–351.

Schmid, S. M., Pfiffner, O. A., Froitzheim, N., Schonborn, G. & Kissling, E. (1996b). Geophysical -geological transect and tectonic evolution of the Swiss-Italian Alps. *Tectonics* **15**, 1036–1064.

Secor, D. T. (1965). Role of fluid pressure in jointing. *American Journal of Science* **263**, 633–

646.

Sharp, Z. . & Kirschner, D. . (1994). Quartz-calcite oxygen isotope thermometry: A calibration based on natural isotopic variations. *Geochimica et Cosmochimica Acta*, 4491–4501.

Sheppard, S. M. F. (1986). Characterization and Isotopic Variations in Natural Waters. *Reviews in Mineralogy* **16**, 165–183.

Sheppard, S. M. F. & Schwarcz, H. P. (1970). Fractionation of carbon and oxygen isotopes and magnesium between coexisting metamorphic calcite and dolomite. *Contributions to Mineralogy and Petrology* **26**, 161–198.

Sibson, R. H. (2000). Tectonic controls on maximum sustainable overpressure: Fluid redistribution from stress transitions. *Journal of Geochemical Exploration* **69–70**, 471–475.

Skelton, A. D. L., Valley, J. W., Graham, C. M., Bickle, M. J. & Fallick, A. E. (2000). The correlation of reaction and isotope fronts and the mechanism of metamorphic fluid flow. *Contributions to Mineralogy and Petrology* **138**, 364–375.

Spötl, C. & Vennemann, T. W. (2003). Continuous-flow isotope ratio mass spectrometric analysis of carbonate minerals. *Rapid communications in mass spectrometry* **17**, 1004–1006.

Suzuoki, T. & Epstein, S. (1976). Hydrogen isotope fractionation between OH-bearing minerals and water. *Geochimica et Cosmochimica Acta* **40**, 1229–1240.

Taylor, B. E. (1986). Magmatic volatiles; isotopic variation of C, H, and S. *Reviews in Mineralogy and Geochemistry*. Mineral Soc America **16**, 185–225.

Taylor, B. E. & Bucher-Nurminen, K. (1986). Oxygen and carbon isotope and cation geochemistry of metasomatic carbonates and fluids-Bergell aureole, Northern Italy. *Geochimica et Cosmochimica Acta* **50**, 1267–1279.

Taylor, H. J. (1977). Water / rock interactions and the origin of H2O in granitic batholiths. *Journal geological society London* **133**, 509–558.

Taylor, H. J. & Sheppard, S. M. F. (1986). Igneous rocks: I. Process of isotopic fractionation and isotope systematics. *Reviews in Mineralogy and Geochemistry* **16**, 227–271.

Taylor, H. P. (1974). The application of oxygen and hydrogen isotope studies to problems of hydrothermal alteration and ore deposition. *Economic Geology* **69**, 843–883.

Trommsdorff, V. & Connolly, J. (1996). The ultramafic contact aureole about the Bregaglia (Bergell) tonalite: Isograds and a thermal model. *Schweizerische Mineralogische Und Petrographische Mitteilungen* **76**, 537–547.

Trommsdorff, V. & Evans, B. W. (1972). Progressive metamorphism of antigorite schist in the Bergell tonalite aureole (Italy). *American Journal of Science*. Kline Geology Laboratory, Yale University **272**, 423–437.

Trommsdorff, V. & Nievergelt, P. (1983). The Bregaglia (Bergell) Iorio intrusive and its field relations. *Mem. Soc. Geol. It* **26**, 55–68.

Veizer, J. & Hoefs, J. (1976). The nature of O18/O16 and C13/C12 secular trends in sedimentary carbonate rocks. *Geochimica et Cosmochimica Acta* **40**, 1387–1395.

Vennemann, T., Fricke, H., Blake, R., O'Neil, J. & Colman, A. (2002). Oxygen isotope analysis of phosphates : a comparison of techniques for analysis of Ag 3 PO 4. *Chemical Geology* **185**, 321–336.

Vennemann, T. W. & O'Neil, J. R. (1993). A simple and inexpensive method of hydrogen isotope and water analyses of minerals and rocks based on zinc reagent. *Chemical Geology* **103**, 227–234.

von Blackenburg, F. (1992). Combined high-precision chronometry and geochemical tracing using accessory minerals: applied to the Central-Alpine Bergell intrusion (central Europe). *Chemical Geology* **100**, 19–40.

von Blanckenburg, F., Früh-Green, G., Diethelm, K. & Stille, P. (1992). Nd-, Sr-, O-isotopic and chemical evidence for a two-stage contamination history of mantle magma in the Central-Alpine Bergell intrusion. *Contributions to Mineralogy and Petrology* **110**, 33–45.

Walther, J. V. & Orville, P. M. (1983). The extraction-quench technique for determination of the thermodynamic properties of solute complexes: application to quartz solubility in fluid mixtures. *American Mineralogist* **68**, 731–741.

Watson, E. B. & Wark, D. A. (1997). Diffusion of dissolved SiO2 in H2O at 1 GPa, with implications for mass transport in the crust and upper mantle. *Contributions to Mineralogy and Petrology* **130**, 66–80.

Wenk, H. R. (1973). The structure of the Bergell Alps. *Eclogae Geol. Helv* **66**, 255–291.

Wenk, H. R., Wenk, E. & Wallace, J. H. (1974). Metamorphic mineral assemblages in pelitic rocks of the Bergell Alps. *Schweizerische Mineralogische und Petrographische Mitteilungen* **54**, 507–554.

Yardley, B. W. D. (2009). The role of water in the evolution of the continental crust. *Journal of the Geological Society, London* **166**, 585–600.

Yardley, B. W. D. & Bottrell, S. H. (1992). Silica mobility and fluid movement during metamorphism of the Connemara schists, Ireland. *Journal of Metamorphic Geology* **10**, 453–464.

Zhao, Z.-F. & Zheng, Y.-F. (2003). Calculation of oxygen isotope fractionation in magmatic rocks. *Chemical Geology* **193**, 59–80.

Zheng, Y.-F. (1993a). Calculation of oxygen isotope fractionation in anhydrous silicate minerals. *Geochimica et Cosmochimica Acta* **57**, 1079–1091.

Zheng, Y. F. (1993b). Calculation of oxygen isotope fractionation in hydroxyl-bearing silicates. *Earth and Planetary Science Letters* **120**, 247–263.

Zheng, Y. F., Metz, P. & Satir, M. (1994a). Oxygen isotope fractionation between calcite and

tremolite: an experimental study. *Contributions to Mineralogy and Petrology* **118**, 249–

255.

Zheng, Y. F., Metz, P., Satir, M. & Sharp, Z. Z. D. (1994b). Experimental calibration of

oxygen isotope fractionation between calcite and tremolite in the presence of a CO2-

H2O. *Chemical Geology* **116**, 17–27.

Zheng, Y. F., Satir, M. & Metz, P. (2004). Oxygen isotope exchange and disequilibrium

between calcite and tremolite in the absence and presence of an experimental C-O-H

fluid. *Contributions to Mineralogy and Petrology* **146**, 683–695.

FIGURE CAPTION

Figure 1: Geologic map of the Bergell intrusion and its environment in the Central Alps. This

area is located at the border between Italy and Switzerland (modified after Schmid et al. 1996;

Müntener et al. 1999).

Figure 2: (a) Example of carbonate xenoliths surrounded by the Bergell tonalites; (b) Same

picture as in (a) with overlay showing xenolith boundaries and vein locations; (c) Hand

sample of a skarn forming at the contact between the dolomites and the tonalites; (d) Close-up

of the skarn formation at the contact between the dolomitic marbles and the tonalites, with

numerous metasomatic reaction veins that form perpendicularly to the contact within the

carbonates and the intrusive rocks; (e) Epidote and quartz vein forming in the tonalites,

surrounded by a replacement zone (endoskarn); (f) Photomicrograph of a thin section of the

endoskarn formed next to the epidote-quartz vein (in cross-polarized light) with interstitial

calcite, epidote and actinolite and rounded quartz and feldspar grains. Abbreviations: act-

actinolite, cc-calcite, di-diopside, do-dolomite, ep-epidote, fo-forsterite, fsp-feldspar, hbl-hornblende, qtz-quartz, serp-serpentine, Ti-clh-titanoclinohumite, tlc-talc, tr-tremolite.

Figure 3: Complex reaction vein showing the succession of reaction zones forming a lobed mineralogical front, which is typical of the forsterite + calcite veins. These veins are suggested to be the result of multiple fluid infiltration events over the cooling history of the system; with repeated failure along the same fracture due to an incomplete seal or an inherited weakness. Mineral abbreviations as in Figure 2; and chl-chlorite.

Figure 4: Stereographic projections of structural data; (a) Reaction veins (poles of planes); and (b) lineations of igneous textures, orientation of sedimentary banding (s0) in the dolomites and contacts between the dolomites and the tonalites (lineations and poles of planes). Grey symbols in (b) represent structural data from Berger and Gieré (1995) of the Val Sissone area. Lambert equal-area projection, lower hemisphere.

Figure 5: (a) Hand sample showing the forsterite and calcite vein used for stable isotope analysis (profile in Fig. 8); calcite stained in red (after Hutchison 1974); (b) Complete cross-section of a tremolite + calcite vein (06-L2), outlining the open fracture central zone framed by symmetrical replacement zones. The two circles drawn onto the vein represent the locations of the samples 06-L2-12 and 06-L2-16; (c) Late talc + calcite veins, showing a shift in the main stress orientation as they do not follow a particular direction, in comparison to the other veins; (d) Hand sample showing the Fe-poor tremolite and calcite vein used for stable isotope analysis (c.f. Figs. 5b and 9); (e) Representative photomicrograph of the replacement zone of the forsterite-calcite vein (cross polarized light); (f) Representative photomicrograph of the central zone and (g) replacement zone of the tremolite-calcite vein (plane polarized light, with calcite stained in red). Mineral abbreviations as in Figure 2; and phl-phlogopite.

Figure 6: (a) Hand sample of an Fe-enriched tremolite and calcite vein (sample 07-L18-2; calcite is stained in red); (b) EPMA element map for Fe from the boundary between the central and the replacement zone. Tremolites from the central zone are enriched in Fe compared to the replacement zone, and so are the rims of the tremolites in the replacement zone. Mineral abbreviations as in Figures 2 and 4.

Figure 7: $\delta^{18}O$ vs. $\delta^{13}C$ values for the dolomite marble and calcites from the forsterite + calcite, tremolite + calcite and talc + calcite veins. The high $\delta^{18}O$ and $\delta^{13}C$ values correspond to the dolomitic protolith, whereas the low $\delta^{18}O$ and $\delta^{13}C$ values represent the calcite from the vein's central and replacement zones. The mixing line (dashed line) represents mechanical mixing of the dolomitic protolith with the vein calcite at the mineralogical replacement front.

Figure 8: Isotopic profile across the forsterite vein (sample 07-L18-4B); $\delta^{18}O$ values for forsterite and carbonates (left axis) and $\delta^{13}C$ values for the carbonates (right axis). Analytical error on the isotopic values is smaller than the size of the symbols. Location of the profile is shown in Figure 5a. The isotope composition in the vein is represented by relatively constant and low values compared to the dolomite protolith; note that the oxygen and carbon isotopic fronts are nearly at the same place, and that both coincide with the vein boundary (solid grey bar), which is also the mineralogical reaction front (see text for explanations). The oxygen value of the carbonates that includes a cross, likely corresponds to spurious data point, and has been excluded from Fig. 7.

Figure 9: Isotopic profile across the Fe-poor tremolite vein (sample 06-L2-16); $\delta^{18}O$ values for tremolite and carbonates (left axis) and $\delta^{13}C$ values for the carbonates (right axis).

Analytical error for the isotopic values is smaller than the size of the symbols. Location of the profile is shown in Figure 5d. The isotopic profile has the same shape as the one for the forsterite vein in Figure 8, with again a perfect overlap of the position of the isotopic fronts relative to the mineralogical front (solid grey bar).

Figure 10: Determination of temperatures for (a) the calcite-forsterite, (b) the calcite-tremolite, (c) the calcite-talc, and (d) the quartz-epidote mineral pairs. These plots show the range of the Δ_{a-b} (in ‰) across the replacement and central zone of the respective veins. The black line is the median, the lower box the 25th percentile (brighter shade of colour), and the upper box the 75th percentile (darker shade); dashed lines represent the minimum and maximum values for Δ_{a-b} and resulting temperatures (see text for explanation; calibrations from Chiba *et al.*, 1989; Matthews and Schliestedt, 1984; Zheng, 1993b; Zheng *et al.*, 1994b, 2004).

Figure 11: $\delta^{18}O$ vs. δD isotope values for talc and tremolite, from the talc vein 07-L30-1 and the tremolite vein 06-L2-16, respectively. Isotopic composition of water (star symbol) in equilibrium with the tremolite (at 390 °C) and talc veins (at 140 °C) calculated from following calibrations; Graham *et al.* (1984); Saccocia *et al.* (2009) and Zheng (1993b). Black line represents the global meteoric water line (GMWL; Craig, 1961); with the grey field being the present day local meteoric water from the GNIP database (2019); fields for metamorphic and primary magmatic water, as well as sediments are plotted after Sheppard (1986). The black dotted line represents the evolution of the isotopic composition of a fluid in equilibrium with igneous rocks with decreasing temperature, using an initial magmatic fluid with an isotopic composition of +9.95 ‰ in $\delta^{18}O$ (von Blanckenburg *et al.*, 1992) and -63 ‰ in δD (calibrations from Suzuoki and Epstein, 1976; Ligang *et al.*, 1989; Zhao and Zheng, 2003).

Figure 12: Calculations of (a) $\delta^{18}O$ of the fluid phase (H_2O) in exchange equilibrium with the veins and with the intrusive rock (using quartz as a proxy), and (b) $\delta^{13}C$ of the fluid phase (CO_2) in equilibrium with the veins. These fluid compositions were calculated using calcite-H_2O, calcite-CO_2 and calcite-quartz fractionations for the forsterite, tremolite and talc veins and average $\delta^{18}O$ and $\delta^{13}C$ values of the calcite measured in the vein; for the epidote-quartz vein, quartz-calcite and quartz-H_2O fractionation with average $\delta^{18}O$ values of quartz were used at the estimated apparent temperatures (Friedman and O'Neil, 1977; Scheele and Hoefs, 1992; Zheng, 1993b; Sharp and Kirschner, 1994). The grey-shaded fields represent the $\delta^{18}O$ and $\delta^{13}C$ range of primary magmatic fluids (after Sheppard, 1986; Taylor, 1986). In (a) the grey lines represent quartz in equilibrium with the tonalite (von Blanckenburg *et al.*, 1992) and the evolution of water in equilibrium with the tonalite with decreasing temperatures (calibrations from Suzuoki and Epstein, 1976; Ligang *et al.*, 1989; Zhao and Zheng, 2003).

Figure 13: (a) Temperature vs. X_{CO2} phase diagram of the system CaO-MgO-SiO_2-H_2O-CO_2 at 0.3 GPa showing relevant mineral reactions. X_{CO2} is the mole fraction of CO_2 in a binary H_2O-CO_2 fluid, and ranges from 0 to 0.1. Inset represents the same phase diagram with X_{CO2} ranging from 0 to 0.5. The system is saturated with calcite and fluid. The blue and yellow fields represent the calculated temperature range for the forsterite and tremolite veins, respectively (interquartile range; Fig. 10); (b) and (c) represent isothermal and isobaric chemical potential diagrams for SiO_2 vs. X_{CO2} for the formation conditions of the forsterite vein (b) and the tremolite vein (c). For metasomatic systems, chemical elements are added and/or removed from the system, controlling their activity. Thus, the chemical potential diagrams (b) and (c) add a dimension to the phase diagram in (a), and show how the stability field of the minerals are influenced by element availability. In (b) forsterite is stable at $\mu(SiO_2)$ values below quartz saturation, and dolomite will become unstable in favour of

forsterite + calcite by either increasing $\mu(SiO_2)$ or decreasing X_{CO2}. Similarly, the tremolite

vein (c) can be formed at $\mu(SiO_2)$ values below quartz saturation, thus not requiring quartz to

be stable in the mineral assemblage. Diagrams constructed with PerpleX (Connolly, 1990),

dataset from Berman (1988) and the equation of state for fluids from Kerrick and Jacobs

(1981); cc-calcite; do-dolomite, di-diopside; fo-forsterite; qtz-quartz; tlc-talc; tr-tremolite.

Figure 14: (a) Mohr-Griffith-Coulomb failure diagram representing extensional failure (star)

(e.g. Secor, 1965; Sibson, 2000; and reviews by Bons et al., 2012). It occurs when the fluid

pressure exceeds σ_3 plus the tensile strengths ($P_f > \sigma_3 + T$; e.g. Secor, 1965; Etheridge, 1983),

shifting the Mohr circle towards the left. (b) Simplified 3-dimensional representation of the

geometry and main stress field around a carbonate xenolith, showing the connectivity

between the reaction veins and the tonalite-xenolith contact; (c) simplified close up of the

tonalite-xenolith contact zones, representing the fluid conduit, with the suggested mass

transfer between the intrusive rocks (to left) and the carbonates (to right) to form the

metasomatized reaction veins. The element transport occurs through diffusion in the fluid

phase. Not to scale.

TABLES

Table 1: Stable isotope composition of carbonates (dolomite and calcite) - profiles

perpendicular to vein direction.

Table 2: Oxygen isotope composition of silicates - profiles perpendicular to vein direction.

Table 3: Hydrogen isotope compositions of tremolite and talc - profiles perpendicular to vein

direction.

Table 4: Calculations of fluid supply and equivalent intrusive rocks needed to react 1 m^3 of pure dolomite in either forsterite + calcite, or tremolite + calcite (using reactions (7) and (8), see text for explanations). Volumes rounded to the nearest tens.
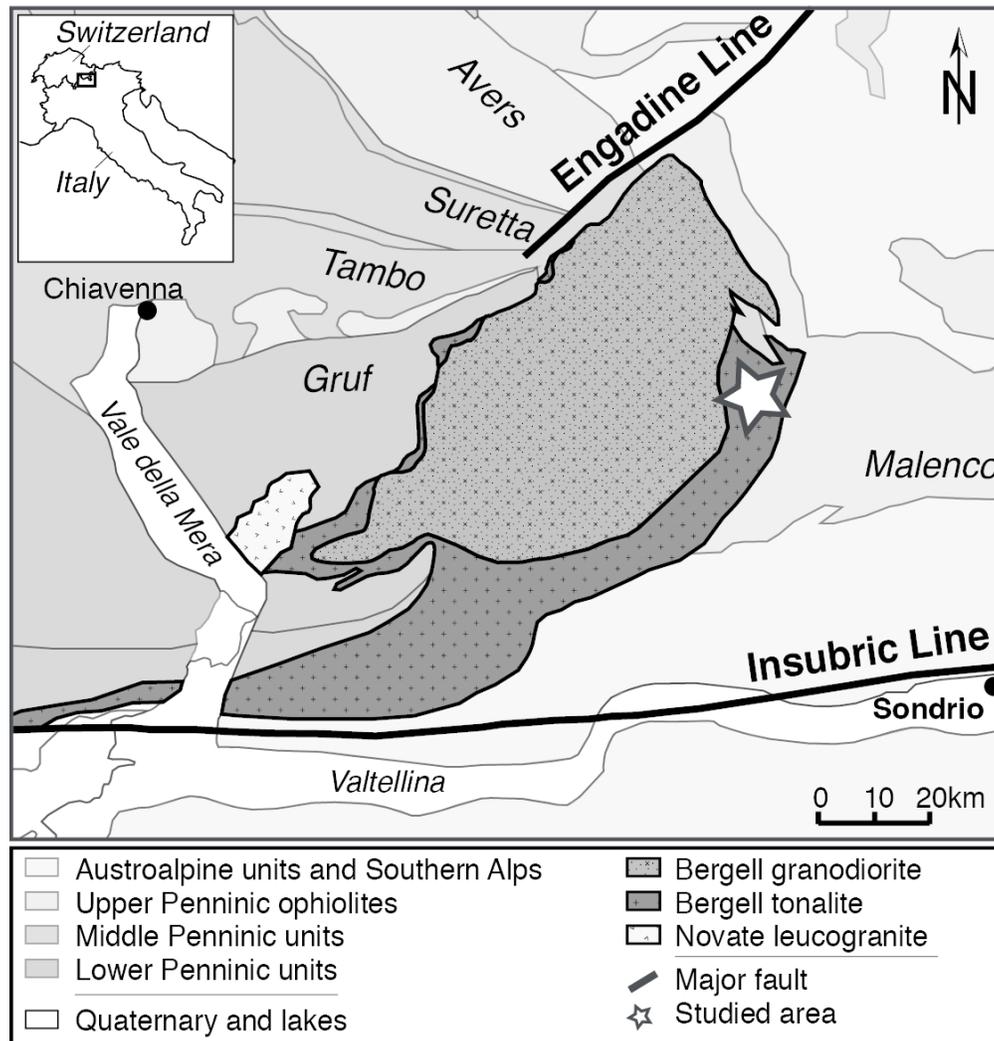
Figure 1: Geologic map of the Bergell intrusion and its environment in the Central Alps. This area is located at the border between Italy and Switzerland (modified after Schmid et al. 1996; Müntener et al. 1999).
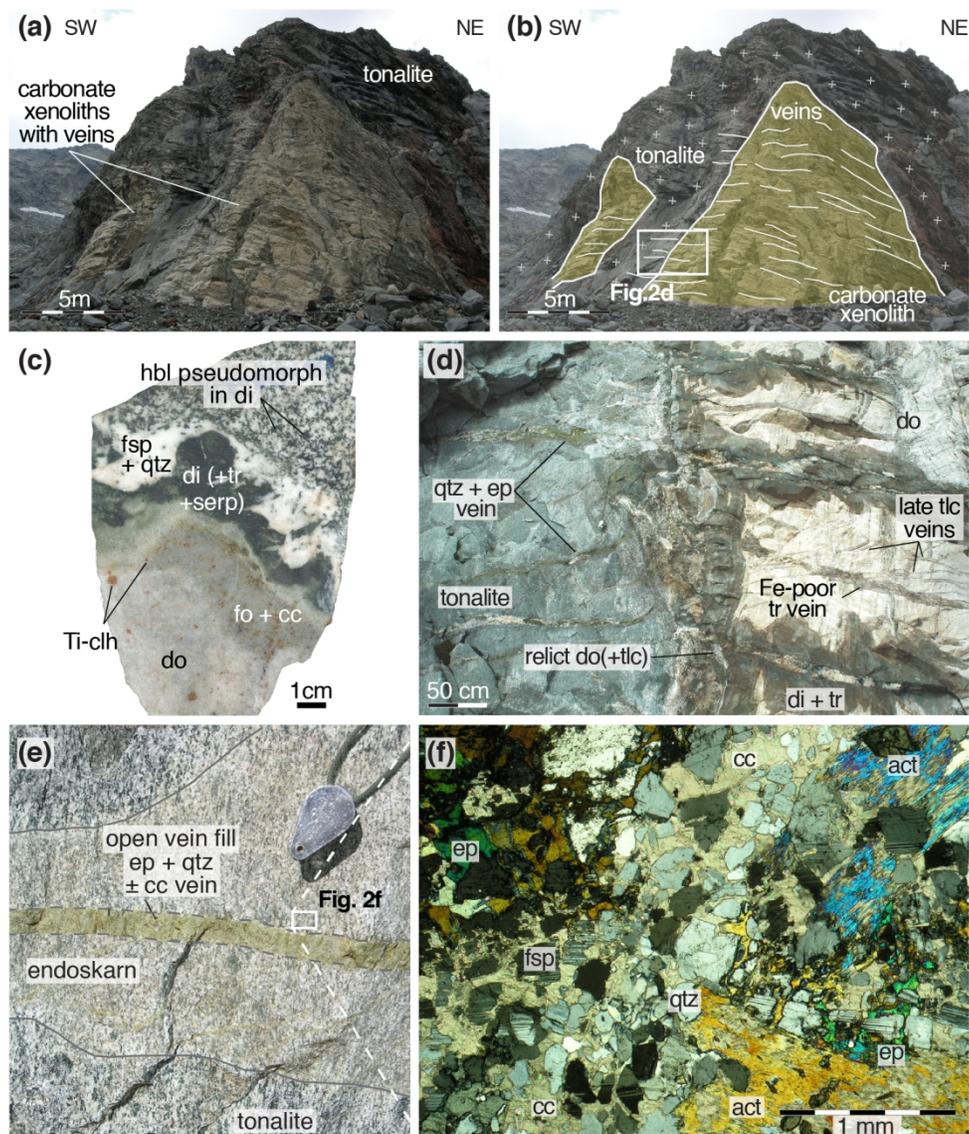
Figure 2: (a) Example of carbonate xenoliths surrounded by the Bergell tonalites; (b) Same picture as in (a) with overlay showing xenolith boundaries and vein locations; (c) Hand sample of a skarn forming at the contact between the dolomites and the tonalites; (d) Close-up of the skarn formation at the contact between the dolomitic marbles and the tonalites, with numerous metasomatic reaction veins that form perpendicularly to the contact within the carbonates and the intrusive rocks; (e) Epidote and quartz vein forming in the tonalites, surrounded by a replacement zone (endoskarn); (f) Photomicrograph of a thin section of the endoskarn formed next to the epidote-quartz vein (in cross-polarized light) with interstitial calcite, epidote and actinolite and rounded quartz and feldspar grains. Abbreviations: act-actinolite, cc-calcite, di-diopside, do-dolomite, ep-epidote, fo-forsterite, fsp-feldspar, hbl-hornblende, qtz-quartz, serp-serpentine, Ti-clh-titanoclinohumite, tlc-talc, tr-tremolite.

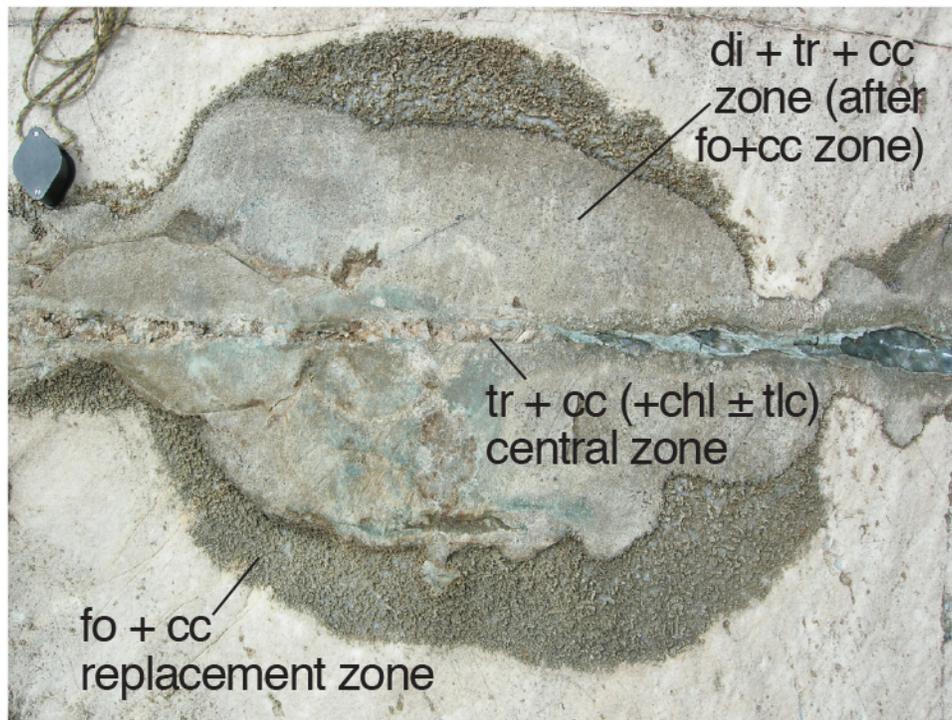Figure 3: Complex reaction vein showing the succession of reaction zones forming a lobed mineralogical front, which is typical of the forsterite + calcite veins. These veins are suggested to be the result of multiple fluid infiltration events over the cooling history of the system; with repeated failure along the same fracture due to an incomplete seal or an inherited weakness. Mineral abbreviations as in Figure 2; and chl-chlorite.

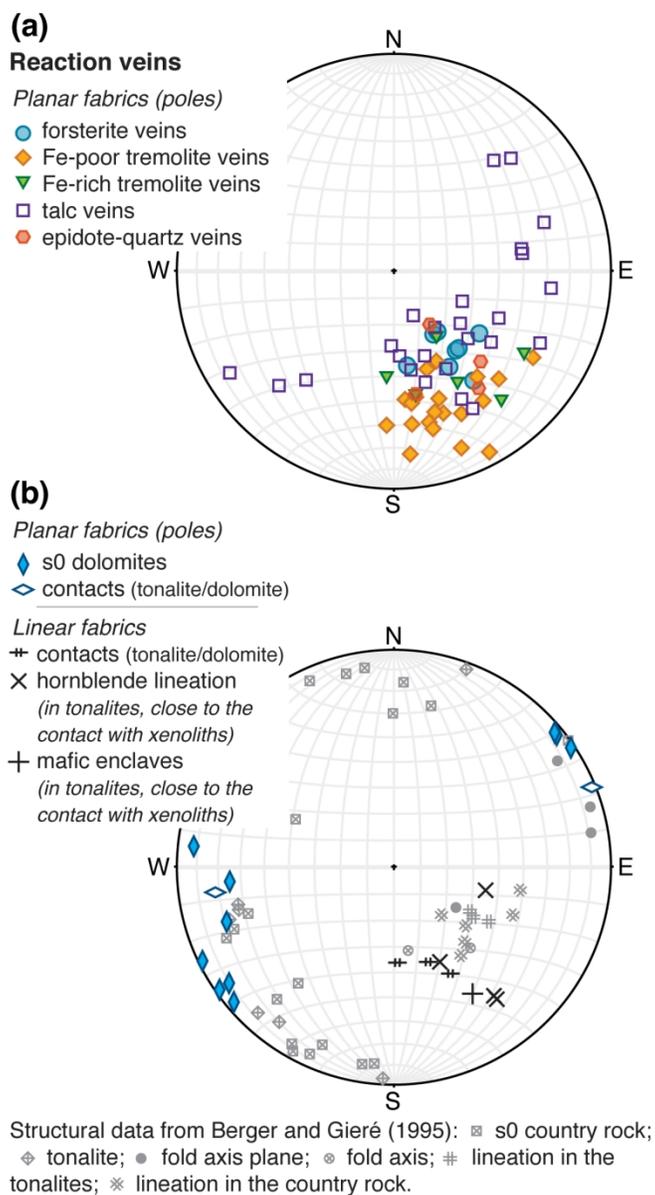Figure 4: Stereographic projections of structural data; (a) Reaction veins (poles of planes); and (b) lineations of igneous textures, orientation of sedimentary banding (s0) in the dolomites and contacts between the dolomites and the tonalites (lineations and poles of planes). Grey symbols in (b) represent structural data from Berger and Gieré (1995) of the Val Sissone area. Lambert equal-area projection, lower hemisphere.
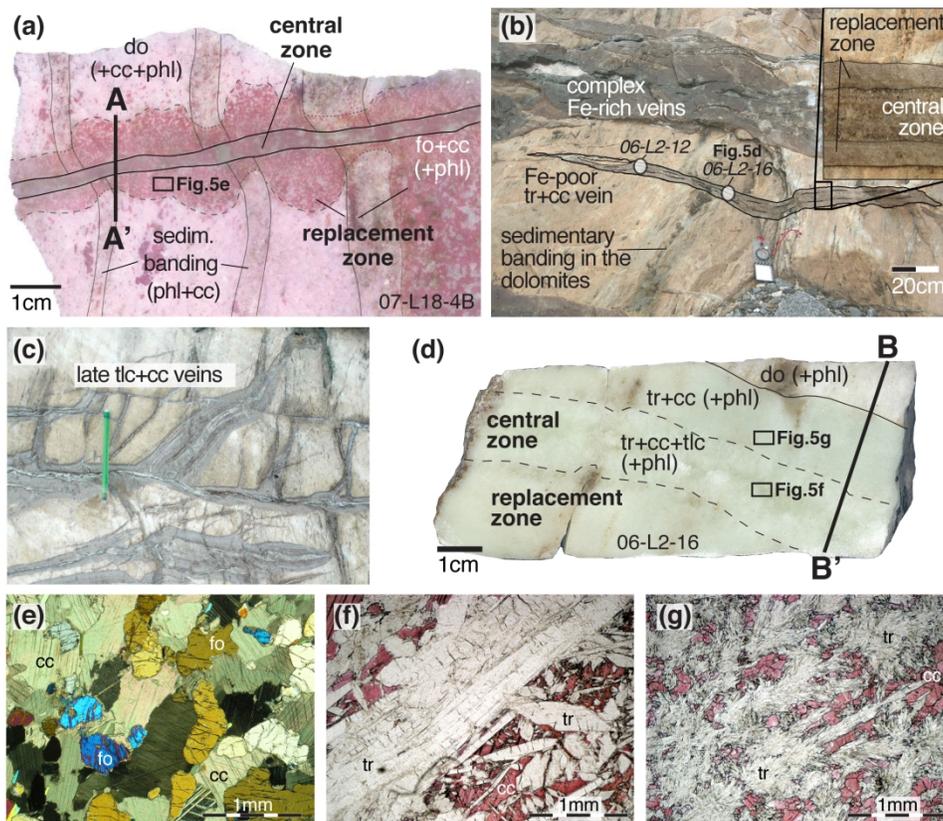
Figure 5: (a) Hand sample showing the forsterite and calcite vein used for stable isotope analysis (profile in Fig. 8); calcite stained in red (after Hutchison 1974); (b) Complete cross-section of a tremolite + calcite vein (06-L2), outlining the open fracture central zone framed by symmetrical replacement zones. The two circles drawn onto the vein represent the locations of the samples 06-L2-12 and 06-L2-16; (c) Late talc + calcite veins, showing a shift in the main stress orientation as they do not follow a particular direction, in comparison to the other veins; (d) Hand sample showing the Fe-poor tremolite and calcite vein used for stable isotope analysis (c.f. Figs. 5b and 9); (e) Representative photomicrograph of the replacement zone of the forsterite-calcite vein (cross polarized light); (f) Representative photomicrograph of the central zone and (g) replacement zone of the tremolite-calcite vein (plane polarized light, with calcite stained in red). Mineral abbreviations as in Figure 2; and phl-phlogopite.

Figure 6: (a) Hand sample of an Fe-enriched tremolite and calcite vein (sample 07-L18-2; calcite is stained in red); (b) EPMA element map for Fe from the boundary between the central and the replacement zone. Tremolites from the central zone are enriched in Fe compared to the replacement zone, and so are the rims of the tremolites in the replacement zone. Mineral abbreviations as in Figures 2 and 4.

Figure 7: $\delta^{18}O$ vs. $\delta^{13}C$ values for the dolomite marble and calcites from the forsterite + calcite, tremolite + calcite and talc + calcite veins. The high $\delta^{18}O$ and $\delta^{13}C$ values correspond to the dolomitic protolith, whereas the low $\delta^{18}O$ and $\delta^{13}C$ values represent the calcite from the vein's central and replacement zones. The mixing line (dashed line) represents mechanical mixing of the dolomitic protolith with the vein calcite at the mineralogical replacement front.

Figure 8: Isotopic profile across the forsterite vein (sample 07-L18-4B); $\delta^{18}O$ values for forsterite and carbonates (left axis) and $\delta^{13}C$ values for the carbonates (right axis). Analytical error on the isotopic values is smaller than the size of the symbols. Location of the profile is shown in Figure 5a. The isotope composition in the vein is represented by relatively constant and low values compared to the dolomite protolith; note that the oxygen and carbon isotopic fronts are nearly at the same place, and that both coincide with the vein boundary (solid grey bar), which is also the mineralogical reaction front (see text for explanations). The oxygen value of the carbonates that includes a cross, likely corresponds to spurious data point, and has been excluded from Fig. 7.

Figure 9: Isotopic profile across the Fe-poor tremolite vein (sample 06-L2-16); $\delta^{18}O$ values for tremolite and carbonates (left axis) and $\delta^{13}C$ values for the carbonates (right axis). Analytical error for the isotopic values is smaller than the size of the symbols. Location of the profile is shown in Figure 5d. The isotopic profile has the same shape as the one for the forsterite vein in Figure 8, with again a perfect overlap of the position of the isotopic fronts relative to the mineralogical front (solid grey bar).

Figure 10: Determination of temperatures for (a) the calcite-forsterite, (b) the calcite-tremolite, (c) the calcite-talc, and (d) the quartz-epidote mineral pairs. These plots show the range of the Δa-b (in ‰) across the replacement and central zone of the respective veins. The black line is the median, the lower box the 25th percentile (brighter shade of colour), and the upper box the 75th percentile (darker shade); dashed lines represent the minimum and maximum values for Δa-b and resulting temperatures (see text for explanation; calibrations from Chiba et al., 1989; Matthews and Schliestedt, 1984; Zheng, 1993b; Zheng et al., 1994b, 2004)

Figure 11: δ^{18}O vs. δD isotope values for talc and tremolite, from the talc vein 07-L30-1 and the tremolite vein 06-L2-16, respectively. Isotopic composition of water (star symbol) in equilibrium with the tremolite (at 390 °C) and talc veins (at 140 °C) calculated from following calibrations; Graham et al. (1984); Saccocia et al. (2009) and Zheng (1993b). Black line represents the global meteoric water line (GMWL; Craig, 1961); with the grey field being the present day local meteoric water from the GNIP database (2019); fields for metamorphic and primary magmatic water, as well as sediments are plotted after Sheppard (1986). The black dotted line represents the evolution of the isotopic composition of a fluid in equilibrium with igneous rocks with decreasing temperature, using an initial magmatic fluid with an isotopic composition of +9.95 ‰ in δ^{18}O (von Blanckenburg et al., 1992) and -63 ‰ in δD (calibrations from Suzuoki and Epstein, 1976; Ligang et al., 1989; Zhao and Zheng, 2003).

Figure 12: Calculations of (a) $\delta^{18}O$ of the fluid phase (H_2O) in exchange equilibrium with the veins and with the intrusive rock (using quartz as a proxy), and (b) $\delta^{13}C$ of the fluid phase (CO_2) in equilibrium with the veins. These fluid compositions were calculated using calcite-H_2O, calcite-CO_2 and calcite-quartz fractionations for the forsterite, tremolite and talc veins and average $\delta^{18}O$ and $\delta^{13}C$ values of the calcite measured in the vein; for the epidote-quartz vein, quartz-calcite and quartz-H_2O fractionation with average $\delta^{18}O$ values of quartz were used at the estimated apparent temperatures (Friedman and O'Neil, 1977; Scheele and Hoefs, 1992; Zheng, 1993b; Sharp and Kirschner, 1994). The grey-shaded fields represent the $\delta^{18}O$ and $\delta^{13}C$ range of primary magmatic fluids (after Sheppard, 1986; Taylor, 1986). In (a) the grey lines represent quartz in equilibrium with the tonalite (von Blanckenburg et al., 1992) and the evolution of water in equilibrium with the tonalite with decreasing temperatures (calibrations from Suzuoki and Epstein, 1976; Ligang et al., 1989; Zhao and Zheng, 2003).

Figure 13: (a) Temperature vs. X_{CO2} phase diagram of the system CaO-MgO-SiO$_2$-H$_2$O-CO$_2$ at 0.3 GPa showing relevant mineral reactions. X_{CO2} is the mole fraction of CO$_2$ in a binary H$_2$O-CO$_2$ fluid, and ranges from 0 to 0.1. Inset represents the same phase diagram with X_{CO2} ranging from 0 to 0.5. The system is saturated with calcite and fluid. The blue and yellow fields represent the calculated temperature range for the forsterite and tremolite veins, respectively (interquartile range; Fig. 10); (b) and (c) represent isothermal and isobaric chemical potential diagrams for SiO$_2$ vs. X_{CO2} for the formation conditions of the forsterite vein (b) and the tremolite vein (c). For metasomatic systems, chemical elements are added and/or removed from the system, controlling their activity. Thus, the chemical potential diagrams (b) and (c) add a dimension to the phase diagram in (a), and show how the stability field of the minerals are influenced by element availability. In (b) forsterite is stable at μ(SiO$_2$) values below quartz saturation, and dolomite will become unstable in favour of forsterite + calcite by either increasing μ(SiO$_2$) or decreasing X_{CO2}. Similarly, the tremolite vein (c) can be formed at μ(SiO$_2$) values below quartz saturation, thus not requiring quartz to be stable in the mineral assemblage. Diagrams constructed with PerpleX (Connolly, 1990), dataset from Berman (1988) and the equation of state for fluids from Kerrick and Jacobs (1981); cc-calcite; do-dolomite, di-diopside; fo-forsterite; qtz-quartz; tlc-talc; tr-tremolite.

Figure 14: (a) Mohr-Griffith-Coulomb failure diagram representing extensional failure (star) (e.g. Secor, 1965; Sibson, 2000; and reviews by Bons et al., 2012). It occurs when the fluid pressure exceeds σ_3 plus the tensile strengths ($P_f > \sigma_3 + T$; e.g. Secor, 1965; Etheridge, 1983), shifting the Mohr circle towards the left. (b) Simplified 3-dimensional representation of the geometry and main stress field around a carbonate xenolith, showing the connectivity between the reaction veins and the tonalite-xenolith contact; (c) simplified close up of the tonalite-xenolith contact zones, representing the fluid conduit, with the suggested mass transfer between the intrusive rocks (to left) and the carbonates (to right) to form the metasomatized reaction veins. The element transport occurs through diffusion in the fluid phase. Not to scale.

Sample		$\delta^{13}C$ (VPDB)	$\delta^{18}O$ (VSMOW)	Distance from vein boundary
		(‰)	(‰)	(mm)
Forsterite vein - 776603 / 129595[a]				**A-A'**
07-L18-4Bc_1	cc	-1.4	17.3	-16.5
07-L18-4Bc_14	cc	-2.6	14.5	-16.0
07-L18-4Bc_2	cc	-3.8	14.8	-15.5
07-L18-4Bc_3	cc	-4.1	13.9	-13.5
07-L18-4Bc_4	cc	-4.3	13.8	-11.5
07-L18-4Bc_5	cc	-4.5	14.0	-9.0
07-L18-4Bc_6	cc	-5.0	13.9	-7.0
07-L18-4Bc_7	cc	-4.6	13.7	-5.5
07-L18-4Bc_8	cc	-4.6	13.6	-4.0
07-L18-4Bc_9	cc	-4.4	13.6	-2.0
07-L18-4Bc_10	cc	-3.2	13.6	-0.5
07-L18-4Bc_13 (vein boundary)	cc	-1.0	18.4	0.0
07-L18-4Bc_11	cc	-0.3	16.6	0.5
07-L18-4Bc_12	do	0.6	22.9	4.0
Tremolite vein (Fe-poor) - 776252 / 130421[a]				**B-B'**
06-L2-16_1	do	0.6	23.1	-10.0
06-L2-16_2	do	0.8	23.4	-7.0
06-L2-16_3	do	0.5	23.1	-6.0
06-L2-16_4	do	0.6	23.1	-4.0
06-L2-16_5	do	0.6	22.7	-3.0
06-L2-16_31	do	0.6	22.3	-2.0
06-L2-16_6	cc	-3.7	15.4	-1.5
06-L2-16_7	cc	-5.9	12.3	-0.5
06-L2-16_32 (vein boundary)	cc	-5.3	12.8	0.0
06-L2-16_8	cc	-5.6	12.7	1.5
06-L2-16_9	cc	-5.7	12.5	2.0
06-L2-16_33	cc	-5.6	12.7	2.3
06-L2-16_10	cc	-5.3	13.5	4.8
06-L2-16_11	cc	-5.5	12.5	5.0
06-L2-16_12	cc	-5.5	12.4	7.5
06-L2-16_13	cc	-5.9	12.6	8.5
06-L2-16_14	cc	-6.0	12.6	10.8
06-L2-16_15	cc	-5.8	12.5	11.0
06-L2-16_16	cc	-6.0	12.5	13.0
06-L2-16_17	cc	-6.1	12.5	14.0
06-L2-16_18	cc	-6.2	12.2	16.0
06-L2-16_19	cc	-6.2	12.2	18.0
06-L2-16_20	cc	-6.2	12.2	18.8
06-L2-16_22	cc	-6.0	12.7	21.3
06-L2-16_23	cc	-6.2	13.1	21.5
06-L2-16_24	cc	-7.3	12.5	23.5
06-L2-16_25	cc	-5.5	12.9	23.5
06-L2-16_26	cc	-6.0	12.4	25.5
06-L2-16_27	cc	-5.9	12.5	25.8
06-L2-16_28	cc	-5.9	12.3	27.5
06-L2-16_29	cc	-6.3	12.5	28.0
06-L2-16_30	cc	-5.9	12.5	30.5
Tremolite vein (Fe-poor) - 776252 / 130421[a]				
06-L2-12-1	do	0.6	24	-7.5
06-L2-12-2	do	0.6	23.9	-5.0
06-L2-12-3	do	0.4	22.4	-1.5
06-L2-12-4 (vein boundary)	cc	-5.1	13.5	0.0

06-L2-12-5	cc	-4.9	14.1	2.0
06-L2-12-6	cc	-5.7	13.2	6.0
06-L2-12-7	cc	-5.1	14.0	9.5
06-L2-12-8	cc	-4.2	15.6	12.0
06-L2-12-9	cc	-5.9	12.5	15.0
06-L2-12-10	cc	-4.7	14.2	16.5
06-L2-12-11	cc	-5.8	12.5	18.0
06-L2-12-12	cc	-5.9	12.3	20.0
06-L2-12-13	cc	-4.5	15.1	22.0
06-L2-12-14	cc	-4.2	15.9	24.0
Tremolite vein (Fe-enriched) - 776603 / 129582[a]				
07-L18-2_1	do	0.7	22.4	-8.0
07-L18-2_2	do	0.8	24.5	-4.0
07-L18-2_3	cc	0.0	16.5	-2.0
07-L18-2_4 (vein boundary)	cc	-4.4	13.7	0.0
07-L18-2_5	cc	-4.9	12.9	6.0
07-L18-2_6	cc	-5.2	12.9	11.5
07-L18-2_7	cc	-5.8	14.1	15.5
07-L18-2_8	cc	-5.3	13.1	18.0
07-L18-2_9	cc	-5.4	12.8	20.0
07-L18-2_10	cc	-5.3	13.0	28.0
07-L18-2_11	cc	-5.7	12.2	31.0
07-L18-2_12	cc	-5.1	12.2	36.5
07-L18-2_13	cc	-4.8	12.9	43.0
Talc vein - 776617 / 129825 [a]				
07-L30-1_1 (vein boundary)	do	1.2	23.5	0.0
07-L30-1_2	cc	-2.2	17.4	1.0
07-L30-1_3	cc	-4.8	13.3	4.0
07-L30-1_4	cc	-5.3	12.8	7.0
07-L30-1_5	cc	-5.5	12.3	8.0
07-L30-1_7	cc	-5.7	12.5	10.0
07-L30-1_8	cc	-5.7	12.4	12.0
07-L30-1_9	cc	-5.2	12.8	13.0
07-L30-1_10	cc	-4.7	13.0	17.0
07-L30-1_11	cc	-3.8	13.4	21.0
07-L30-1_12	cc	-2.6	17.2	22.0
07-L30-1_16 (vein boundary)	cc	0.3	22.4	22.5
07-L30-1_13	do	1.4	24.8	23.0
07-L30-1_14	do	1.5	25.5	26.0
07-L30-1_15	do	1.5	25.5	29.0

[a] CH1903 coordinates

Sample	Weight	δ¹⁸O (VSMOW)	Distance from vein boundary
	(mg)	(‰)	(mm)
Forsterite vein - 776603 / 129595[a]			**A-A'**
07-L18-4B_ol11	0.72	9.1	-16.0
07-L18-4B_ol9	0.98	9.1	-14.0
07-L18-4B_ol2	0.8	9.1	-13.0
07-L18-4B_ol12	0.83	9.0	-12.0
07-L18-4B_ol3	0.96	9.1	-11.0
07-L18-4B_ol5	1.41	11.1	-7.0
07-L18-4B_ol6	0.47	9.8	-5.0
07-L18-4B_ol14	1.04	9.3	-4.0
07-L18-4B_ol7	1.23	11.1	-3.0
07-L18-4B_ol10	0.85	10.3	-2.0
07-L18-4B_ol8	0.36	9.1	-1.0
			B-B'
Tremolite vein (Fe-poor) - 776252 / 130421[a]			
06-L2-16_tr1	1.13	8.6	0.0
06-L2-16_tr2	1.15	8.7	2.0
06-L2-16_tr3	0.39	8.6	3.0
06-L2-16_tr4	1.04	8.4	4.0
06-L2-16_tr5	0.65	9.1	6.0
06-L2-16_tr6+7	0.63	8.2	12.0
06-L2-16_tr8	0.6	8.6	17.0
06-L2-16_tr9	0.91	8.6	24.0
06-L2-16_tr10	1.11	8.6	26.0
Epidote – Quartz vein - 776252 / 130421[a]			
Epidote			
07-L2-24_ep1a	1.07	7.6	--
07-L2-24_ep1b	1.51	7.3	--
07-L2-24_ep2	1.15	7.6	--
07-L2-24_ep3	1.4	7.7	--
07-L2-24_ep4	1.28	7.3	--
Quartz			
07-L2-24_qtz1	1.34	11.9	--
07-L2-24_qtz3	1.05	10.7	--
07-L2-24_qtz4	1.46	11.7	--
07-L2-24_qtz5	1.41	11.7	--
Talc vein - 776617 / 129825[a]			
07-L30-1_tlc1	0.68	9.7	1.0
07-L30-1_tlc2	1.2	9.1	3.0
07-L30-1_tlc3	1.18	9.1	5.0
07-L30-1_tlc4	1.07	9.1	7.0
07-L30-1_tlc5	0.45	12.4	9.0
07-L30-1_tlc6	1.45	9.4	11.0
07-L30-1_tlc7	0.76	9.8	13.0
07-L30-1_tlc10	1.49	8.8	21.0

[a] CH1903 coordinates

Sample	Weight	δD (VSMOW)	H2O
	(μg)	(‰)	(wt.%)
Tremolite vein (Fe-poor) - 776252 / 130421[a]			
06-L2-16_H1a	2545	-69	2.37
06-L2-16_H1b	2475	-68	2.30
06-L2-16_H2a	2441	-69	2.57
06-L2-16_H2b	2503	-71	2.56
06-L2-16_H3a	2426	-68	2.36
06-L2-16_H3b	2558	-68	2.43
Talc vein - 776617 / 129825 [a]			
07-L30-1_H1a	1527	-69	4.11
07-L30-1_H1b	1428	-66	4.04
07-L30-1_H2a	1622	-68	4.32
07-L30-1_H2b	1334	-66	4.34
07-L30-1_H3a	850	-58	4.22

[a] CH1903 coordinates

Table 4 Calculations of fluid supply and equivalent intrusive rocks needed to react 1 m³ of pure dolomite in either forsterite + calcite, or tremolite + calcite (using reactions (7) and (8), see text for explanations). Volumes rounded to the nearest tens.

		Fo-vein	**Tr-vein**
P	GPa	0.3	0.3
T	°C	555	390
X_{CO2} [a]		0.05	0.01
Molar volume H_2O [b]	cm³/mol	24.70	20.97
Molar volume CO_2 [b]	cm³/mol	51.60	45.81
H_2O from 1m³ of intrusive rock [c]	mol	7.5×10^3	7.5×10^3
	m³	0.19	0.16
Dolomite consumed (1m³)	mol	1.6×10^4	1.6×10^4
CO_2 produced [d]	mol	1.6×10^4	2.2×10^4
	m³	0.8	1.0
H_2O needed to maintain constant X_{CO2} [e]	**mol**	**3.0×10^5**	**2.2×10^6**
	m³	**7**	**45**
Vol. of intrusive rock to produce required H_2O [c]	**m³**	**40**	**290**
m SiO_2(aq) [f]	mol/kg	0.1438	0.0424
H_2O needed to transport the required SiO_2(aq)	mol	3.0×10^6	3.3×10^7
	m³	74	680
Vol. of intrusive rock to produce enough H_2O to dissolve required SiO_2 [c]	m³	400	4'350

Left vertical labels for the upper section: **STATIONARY FLUID MODEL -DIFFUSION (model proposed in this study)**; **Maintaining constant X_{CO2}**

Left vertical labels for the lower section: ONE-PASS FLUID-FLUSHING MODEL; Using SiO_2(aq) solubility in pure H_2O fluid; Quartz saturated conditions

[a] from phase petrology (Fig. 13)
[b] using the Pitzer and Sterner (1994) equation of state for fluids
[c] with a density for the intrusive rocks of $2.7 \times 10^{+6}$ g/m³ and 5 wt.% water loss
[d] CO_2 produced by the reactions (7) and (8)
[e] H_2O needed to maintain X_{CO2} at initial values using equation (6), calculated after Ferry (1980)
[f] solubility of SiO_2(aq) in pure H_2O calculated from Manning (1994)